

**Local changes in the microstructure, mechanical and electrochemical properties of friction stir welded joints from aluminium of varying grain size**

Orłowska, Marta; Pixner, Florian; Hütter, Andreas; Kooijman, Agnieszka; Jasiński, Cezary; Gonzalez-Garcia, Yaiza; Enzinger, Norbert; Lewandowska, Małgorzata

**DOI**

[10.1016/j.jmrt.2021.11.057](https://doi.org/10.1016/j.jmrt.2021.11.057)

**Publication date**

2021

**Document Version**

Final published version

**Published in**

Journal of Materials Research and Technology

**Citation (APA)**

Orłowska, M., Pixner, F., Hütter, A., Kooijman, A., Jasiński, C., Gonzalez-Garcia, Y., Enzinger, N., & Lewandowska, M. (2021). Local changes in the microstructure, mechanical and electrochemical properties of friction stir welded joints from aluminium of varying grain size. *Journal of Materials Research and Technology*, 15, 5968-5987. <https://doi.org/10.1016/j.jmrt.2021.11.057>

**Important note**

To cite this publication, please use the final published version (if applicable).  
Please check the document version above.

**Copyright**

Other than for strictly personal use, it is not permitted to download, forward or distribute the text or part of it, without the consent of the author(s) and/or copyright holder(s), unless the work is under an open content license such as Creative Commons.

**Takedown policy**

Please contact us and provide details if you believe this document breaches copyrights.  
We will remove access to the work immediately and investigate your claim.

Available online at [www.sciencedirect.com](http://www.sciencedirect.com)

**jmr&t**  
Journal of Materials Research and Technology  
journal homepage: [www.elsevier.com/locate/jmrt](http://www.elsevier.com/locate/jmrt)



## Original Article

# Local changes in the microstructure, mechanical and electrochemical properties of friction stir welded joints from aluminium of varying grain size



Marta Orłowska <sup>a,\*</sup>, Florian Pixner <sup>b</sup>, Andreas Hütter <sup>b</sup>,  
Agnieszka Kooijman <sup>c</sup>, Cezary Jasiński <sup>d</sup>, Yaiza Gonzalez-Garcia <sup>c</sup>,  
Norbert Enzinger <sup>b</sup>, Małgorzata Lewandowska <sup>e</sup>

<sup>a</sup> Military University of Technology, Faculty of Mechanical Engineering, Kaliskiego 2, 00-908, Warsaw, Poland

<sup>b</sup> Graz University of Technology, Institute of Materials Science, Joining and Forming, Kopernikusgasse 24/I, 8010, Graz, Austria

<sup>c</sup> Delft University of Technology, Department of Materials Science and Engineering, Mekelweg 2, 2628 CD, Delft, the Netherlands

<sup>d</sup> Warsaw University of Technology, Faculty of Production Engineering, Narbutta 85, 02-524, Warsaw, Poland

<sup>e</sup> Warsaw University of Technology, Faculty of Materials Science and Engineering, Wołoska 141, 02-507, Warsaw, Poland

## ARTICLE INFO

## Article history:

Received 9 August 2021

Accepted 10 November 2021

Available online 17 November 2021

## Keywords:

Aluminium

Friction stir welding

Ultrafine-grained microstructure

Local characterization

Mechanical properties

Microcapillary

## ABSTRACT

The present study shows results of friction stir welded (FSW) samples after different plastic deformation routes. The welds were made of coarse-grained and ultrafine-grained commercially pure aluminium. As a plastic deformation method a new hybrid process has been chosen, which resulted in obtaining samples with different characteristics of microstructure, which also differed in dependence of the examined plane. Microstructure observations showed that, regardless of the base material, due to continuous dynamic recrystallization a stir zone was characterized by equiaxial grains with an average size of 3.5–5.0  $\mu\text{m}$ . However, significant differences in the changes of the microstructure in thermomechanically affected and heat affected zones have been obtained between welds. Microhardness profiles revealed a decrease in the stir zones in comparison with the initially deformed samples, but an increase for the annealed samples. Tensile tests showed differences between the samples. In the deformed samples, the rupture occurred in a stir zone, while in the undeformed samples in the base material. In addition, due to the application of 3D digital image correlation, it was possible to observe deformation and local changes between the weld zones during the tensile test. Additionally, local electrochemical measurements were performed with two sizes of working electrode, which included the application of microcapillary technique. The results showed higher corrosion resistance in 3.5% NaCl in the stir zones.

© 2021 The Author(s). Published by Elsevier B.V. This is an open access article under the CC BY license (<http://creativecommons.org/licenses/by/4.0/>).

\* Corresponding author.

E-mail address: [marta.orlowska@wat.edu.pl](mailto:marta.orlowska@wat.edu.pl) (M. Orłowska).

<https://doi.org/10.1016/j.jmrt.2021.11.057>

2238-7854/© 2021 The Author(s). Published by Elsevier B.V. This is an open access article under the CC BY license (<http://creativecommons.org/licenses/by/4.0/>).

## 1. Introduction

Friction stir welding (FSW) [1] is a solid-state welding technique by which metallic plates or sheets can be joined together. A solid weld is achieved through a mixing of plasticized materials by intensive plastic deformation at a temperature lower than the melting point of the welded materials. FSW provides a unique combination of large strain, high temperature and high strain rate that results in both unique performance and complex microstructural changes such as grain structure, texture, phase transformation and dispersion of intermetallic compounds [2]. The welds obtained are characterized by four specific zones in which different changes in the microstructure occur: (i) base material (BM); (ii) heat-affected zone (HAZ); (iii) thermomechanically affected zone (TMAZ) and (iv) in the center of the weld, nugget or stir zone (SZ). Due to plastic deformation at elevated high temperature, dynamic recrystallization (DRX) may occur in this area, resulting in equiaxed grains a few microns in size. Applied process parameters determine the microstructure and properties of welds, as was summarized in details in a review paper [3].

In the literature, a large number of works can be found on welding aluminium (Al) alloys using FSW, e.g. [4,5]. FSW is a well-established method, and the microstructural changes it induces have been described in detail for coarse-grained (CG) materials [6]. However, the changes in properties which are caused by FSW are mainly examined in a global manner. It could be seen in case of examining corrosion resistance in the weld zones, since complex changes in microstructure also affect electrochemical behavior [7]. Due to their properties, FSW welds display enhanced corrosion resistance in comparison with the commonly applied welding techniques used for welding Al components. Immersion tests in 3.5% NaCl of welds of AA6xxx obtained by FSW and the metal inert gas (MIG) method have shown that FSW results in better corrosion resistance [8]. Both welds experienced pitting corrosion, but for FSW there was no difference between zones, while for MIG the interfaces around the thermally affected zone were the most critical. The enhanced corrosion resistance of the FSW joint has been attributed to its more homogenous microstructure, including the distribution of intermetallic particles [8]. For MIG welds, the heat input caused a coarsening of grains along with a partial dissolution of the intermetallics that re-precipitated at grain boundaries; this together with high porosity, has a detrimental impact on corrosion resistance. Furthermore, a FSW weld of AA5083 showed a significant improvement in corrosion resistance in comparison to a weld obtained by the tungsten inert gas (TIG) method [9]. The TIG weld was more susceptible to both intergranular and exfoliation corrosion compared with BM, but also with the FSW joint. This was caused by the high heat input during TIG welding, which resulted in coarser grain structures and the precipitation of phase  $\beta$ Al-Mg (aluminium – magnesium intermetallic compounds) at grain boundaries, which makes them susceptible to corrosion. Also, in [10] the corrosion resistance was higher for an FSW weld than for a TIG weld of AA2014, as the TIG welding resulted in a dissolution and coarsening of the precipitates, which in turn reduced the

corrosion resistance. Moreover, FSW can improve the corrosion resistance of the material, as was shown for 2xxx Al alloys [11]. It was mainly attributed to solid solution and precipitation evolution of high equilibrium potential elements, which resulted in microstructure with enhanced corrosion resistance in comparison to the base materials.

Not only corrosion properties are changed by FSW, but also mechanical properties. Therefore, due to preserving the solid state during welding, FSW is also a promising method for joining thermally unstable materials, such as ultrafine-grained (UFG) ones, which can be obtained by the group of methods known as severe plastic deformation (SPD) [12] or other novel techniques such as deformation-driven metallurgy [13]. In our previous works [14,15], we investigated the influence of initial microstructure on the microstructure and properties of SZ for commercially pure Al. It was shown that, due to the DRX, grain growth in the weld occurred which caused a decrease in microhardness and mechanical strength in comparison with the base UFG material. However, the strength obtained of the UFG joints was higher than for the annealed material. Similar findings have been made in other works on this topic. For UFG commercially pure Al and 6016 Al alloy [16], welding using FSW caused a decrease in microhardness in SZ to a value similar to that of undeformed materials. For age-hardening UFG Al–Cu–Mg–Ag alloy, it was shown that, by a combination of FSW and ageing, high mechanical strength could be preserved after welding [17].

It should be emphasized that, although microstructure is mostly investigated locally, properties (both mechanical and corrosion) are usually determined globally. In this paper, we would like to change this perspective and propose a new approach, i.e. that of investigating welds in a local manner, which will allow to distinguish differences and resolve local properties between particular weld zones. The aim of this study, then, is to examine local changes in mechanical and electrochemical properties and correlate them with changes in the microstructure of welds from CG and UFG commercially pure Al. The paper shows a comprehensive approach to characterizing welds after FSW and describe the changes that take place in relation to the degree of deformation of the base material.

This work shows two aspects of the newness – the selection of chosen welding materials and the approach to characterizing the welds. In the case of the first aspect, it is a very first work in which samples after chosen deformation routes have been welded. These samples exhibit different characteristic of the microstructure between each other but also on transverse and normal planes. The results obtained in the present study broaden the knowledge of welding plastically deformed materials, which are thermally unstable. Changes in a microstructure not only in a SZ, but in all characteristic for FSW zones have been investigated. Results have revealed, how the initial microstructure influences the microstructural changes in particular welds areas. The second aspect comes from the approach, in which microstructure, mechanical properties and corrosion resistance characteristics of the welds were studied not only globally but also locally. It allows for a comprehensive description of the materials and a detailed insight into the phenomena taking place during selected processes of plastic deformation, as well as welding.

The combination of the applied techniques allowed for a detailed characterization of the welds and analysing changes in microstructure with mechanical and electrochemical properties.

## 2. Materials and methods

As the material for investigation, commercially pure Al (min. 99.50 wt.% of Al) delivered from Aluminium Konin steelwork was chosen. Samples in the form of hot extruded bars were machined and processed in a hybrid process. An idea of the processing has been presented in our previous work [18]. It consists of multi-turn equal channel angular pressing (mtECAP) [19] with subsequent upsetting (E + U). The scheme of the hybrid SPD process has been illustrated in Fig. 1. The mtECAP (Fig. 1a) is based on pressing the billet through a channel with two angles of  $\phi = 90^\circ$  at room temperature (RT). Four passes of route C (rotation of  $180^\circ$  between passes) were performed with subsequent multistroke flat die upsetting (Fig. 1b) from 26 to 3 mm, resulting in a total equivalent strain of  $\epsilon = 12.6$ . Additionally, a sample after conventional metal forming process, which is flat die upsetting (U) at an equivalent strain of  $\epsilon = 3.4$  was also investigated. Together with the initial, i.e. annealed sample (A), it gave three stocks of flat Al (base materials).

Three similar welds (i.e. A–A, U–U and E + U–E + U) were prepared using the FSW method, with the same tool and the same welding parameters. The scheme of the FSW process is presented in Fig. 2. A tool with a flat shoulder with a diameter (d) of 12 mm and a cylindrical tapered pin with a thread and length of 2.85 mm, and a diameter of from 5 to 3.5 mm, was used. The tool plunge depth was 0.15 mm, the axial force was ~6 kN. The FSW was stroke-controlled with a rotational speed (n) of 800 rpm and a linear speed (V) of 400 mm/min. The selection of welding parameters was based on the literature data, but also on the preliminary tests. With chosen rotational speed, the applied linear speed was the optimal in which defect-free weld has been obtained. The tilt angle of the tool ( $\alpha$ ) was  $1.5^\circ$ .

For a detailed microstructure characterization of the welds and base materials, electron backscatter diffraction (EBSD) on an analytical scanning electron microscope (SEM) Hitachi Su70 was performed, equipped with the Gatan MonoCL 3 CL spectrometer and the HKL Channel5 EBSD setup. The EBSD analysis were performed with an accelerated voltage of 20 kV, sample inclination of  $70^\circ$ , and a step size of 250 nm. The cleaning procedure was performed via ‘noise reduction’ of

free pixels option in used software. The limit misorientation for the grain detection was set for  $3^\circ$ . Additionally, for the BM, observations on a Jeol Jem 1200 transmission electron microscope (TEM) were conducted. For both investigations, the samples were prepared by electropolishing on a Struers Tenupol-5 at a voltage of 35 V and a temperature of 278 K. A standard electrolyte for Al and its alloys was used. The observations were carried out on the normal and transverse planes of the plates (see Fig. 2). From the EBSD measurements, the following data were designated: (i) average grain size (d), defined as the equivalent diameter of a circle with the same area as a measured grain [20]; (ii) distribution of grain boundaries misorientation angles; and (iii) fraction of high angle grain boundaries (HAGB), defined as boundaries with a misorientation angle above  $15^\circ$ , while low angle grain boundaries (LAGB) were defined as those with a misorientation angle of above  $2^\circ$  and less or equal to  $15^\circ$ . Moreover, orientation maps (OIM) and maps of grain boundaries were collected and analyzed. For the microtexture analysis free ATEX software [21] has been used. Texture analysis was based on {111} pole figures (PF). For SZ the rotation has been performed with the ideal shear deformation reference frame, in which textures were described by alignment of the crystallite lattices with the shear plane normal (SPN) and the shearing direction (SD).

Mechanical properties were examined by means of tensile tests, using fivefold rectangular flat samples. The tests were conducted using non-contact displacement measurement with 3D digital image correlation (DIC). The tests were carried out at RT with a strain rate of  $1 \times 10^{-3} \text{ s}^{-1}$ . Representative curves of the engineering stress–strain for the welds, and for the BMs as well, are presented. The average values of the ultimate tensile strength (UTS) and elongation to break (E) were determined. Additionally, deformation maps showing the places of strain localization during tensile straining were plotted. The welds were tested in the as-welded condition. Additionally, in order to distinguish the changes across the welds, line scans of the microhardness measurements were performed on the centre lines of the transverse and normal sections. The Vickers method was used, with a load of 100 g (HV0.1). The loading time was 15 s and the step size of the measurements was 250  $\mu\text{m}$ .

Electrochemical properties were examined using potentiodynamic polarization (PP) tests in naturally aerated 3.5 wt.% NaCl. A standard three-electrode system was used with a platinum wire as the counter electrode, an Ag/AgCl electrode as the reference electrode, and the examined sample as the

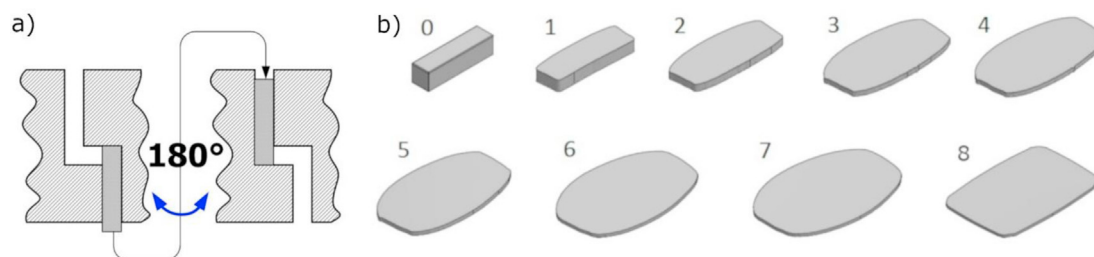


**Fig. 1 – Production of an upset stock of flat Al (for samples E + U): a) schematics of mtECAP (applied in the first stage of the hybrid SPD process), b) multistroke upsetting process (performed in the second stage of the hybrid SPD process).**

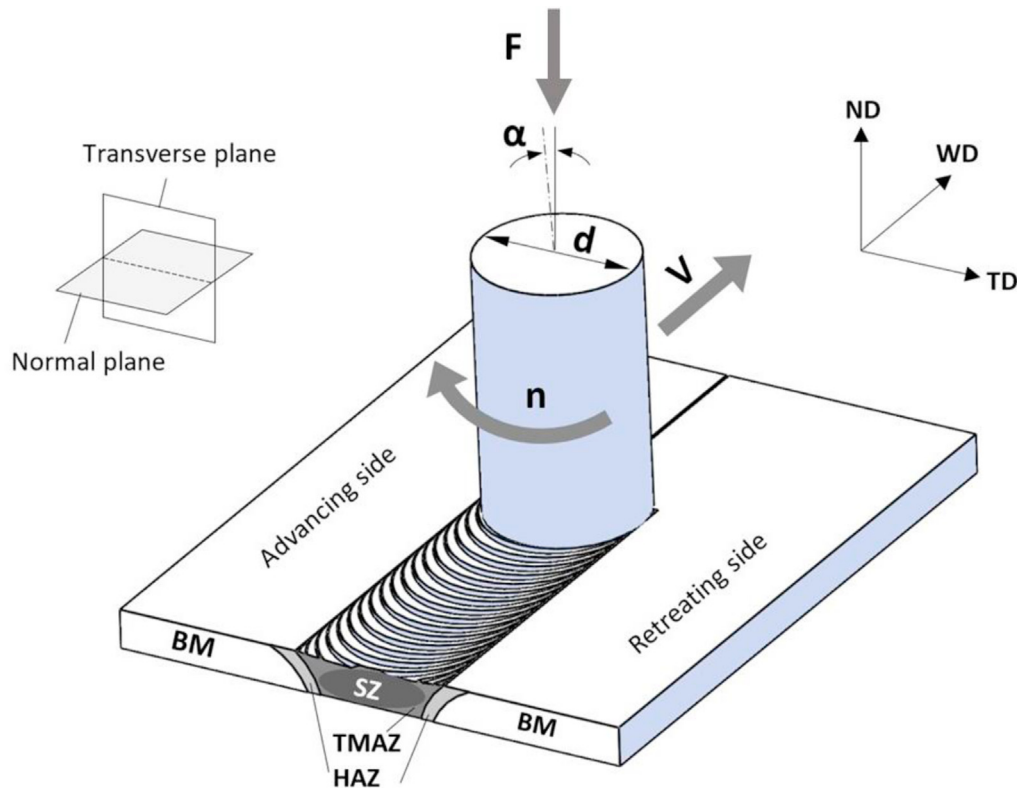


Fig. 2 – The scheme of the FSW process together with marked examined planes.

working electrode. With a standard cell, the area examined, which had a diameter of 1 mm (surface area of  $7.85 \times 10^{-3} \text{ cm}^2$ ), was measured. Measurements of SZ and BM for each weld were taken on their transverse sections. Additionally, for detailed investigations of each weld zone, tests were run with a microcapillary cell [22]. A microcapillary with a diameter of 250  $\mu\text{m}$  (surface area of  $5 \times 10^{-4} \text{ cm}^2$ ) was used. The experiments were performed on the cross-sections of each weld, in four areas: (i) BM; (ii) HAZ; (iii) TMAZ and (iv) SZ. At least three measurements per zone were made. Electrochemical parameters: (i) corrosion potential ( $E_{\text{corr}}$ ) and (ii) corrosion current density ( $i_{\text{corr}}$ ) were designated from a Tafel extrapolation. PP scans for both experiments were performed from 0.05 V below to 0.5 V above the open circuit potential, at a scan rate of 2 mV/s. An SP 200 Bio-Logic Potentiostat was used. Afterwards, the surfaces of the samples were examined using a Jeol JSM-IT100 SEM. The samples prior to the measurements were ground and polished with a diamond suspension with a final size of 1  $\mu\text{m}$ .

### 3. Results

#### 3.1. Microstructure

OIMs of sample A in two perpendicular planes are shown in Fig. 3, while the quantitative results are gathered in Table 1. Sample A shows grains with an average size of about 20  $\mu\text{m}$  and a fraction of HAGBs of 79%. In both planes, the grain size is

comparable and their shape is close to equiaxial. OIMs together with representative TEM micrographs of the samples after plastic working are presented in Fig. 4. Application of plastic deformation caused a significant reduction in grain size and changes in the fraction of HAGBs. The transverse planes feature elongated grains with an average size of 1.1  $\mu\text{m}$  and 0.8  $\mu\text{m}$  for the U and E + U samples, respectively. In the normal plane, the grains are equiaxial with a slightly higher average grain size of 2.5  $\mu\text{m}$  and 1.5  $\mu\text{m}$  for samples the U and E + U, respectively. The observed variability in grain size is due to the fact that grains (with misorientation angle above  $15^\circ$ ) and subgrains ( $>3^\circ$ ) were taken into account while the average grain size was calculated. As the subgrains size is smaller, it is responsible for reducing the average grain size, however the variability is increased. The shape of the grains is a direct consequence of the upsetting process, which causes them to be flattened into ‘pancakes’, but also causes a further grain refinement. As for the characteristics of the grain boundaries, it should be noted that for the U sample, the fraction of HAGBs is about 40%, while for the E + U samples, HAGBs dominate, constituting about 80% of all grain boundaries.

OIMs together with grain boundary arrangements taken from the transverse and normal planes of the welds are presented in Fig. 5 and in Fig. 6, respectively. The maps illustrate microstructural changes from the BM to SZ taken on the advancing side of the welds. The quantitative results of average grain size together with the fraction of HAGBs are gathered in Table 1. It should be noted that the SZs feature a very similar equiaxial microstructure, with the average grain

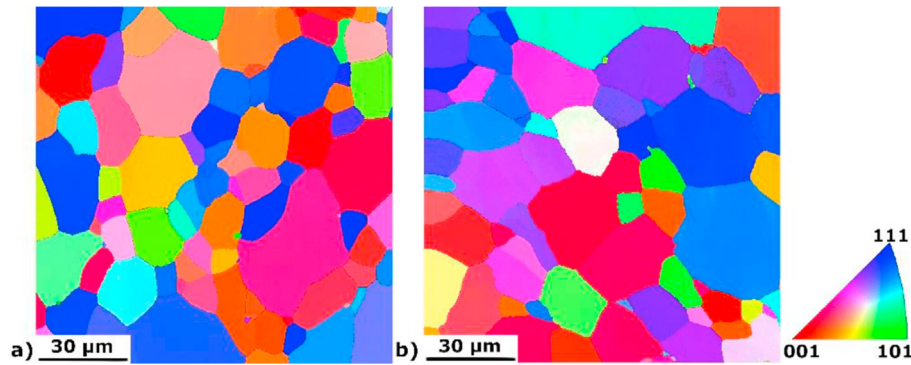


Fig. 3 – OIM of sample A in planes: a) transverse and b) normal.

size ranging from 3.5 to 4.9  $\mu\text{m}$  for both planes and for all three welds. This indicates that the FSW process changes the microstructure from elongated to equiaxial for the U and E + U samples, where the grains were highly flattened after the upsetting process. Another observation is that the grain size in the SZ is independent of the microstructure of the BM. Therefore, there is no correlation between grain size in the BM and SZ. For all three welds, the grains in the SZ are of comparable size, which means that they are more dependent on the applied welding parameters. The HAZ/TMAZ areas reveal comparable grain size values, but with the biggest variety (i.e. standard deviation) in the A–A weld. For this weld, a gradual decrease in grain size can be noticed from the BM to the SZ. For the U–U and E + U–E + U welds, there is an opposite correlation: the grain size increases in the direction of the SZ.

Aside from grain size, the arrangement and misorientation angles of the grain boundaries also vary, depending on the location on the weld. For the A–A weld, the BM features coarse equiaxial grains with HAGBs. For the U–U weld, the grains in the BM are elongated in the transverse plane, with HAGBs as geometrically necessary boundaries and LAGBs as transverse boundaries, which are incidental dislocation boundaries [23] (see Fig. 4). For the E + U–E + U weld, the fraction of HAGBs in the BM is significantly increased. The fractions of HAGBs in each zone for each weld are listed in Table 1, while the distribution of grain boundaries misorientation angles taken

from the transverse sections are presented in Fig. 7. A Mackenzie plot is added to each graph (marked as a black line). It is a theoretical plot for randomly oriented grains in polycrystals [24]. The graphs do not match this curve for any of the samples, indicating the presence of some texture components. For the A–A weld, the misorientation distribution varies the most for the TMAZ/HAZ zone, where a higher fraction of LAGBs can be observed. As a result, in this area the fraction of HAGBs is the lowest, at 65%, while in the SZ it increases significantly, up to a value of around 80%. In case of the U–U weld, there is a constant increase in the fraction of HAGBs in the direction of the SZ, up to about 76%. For the E + U–E + U weld, the fraction of HAGBs is stable over the whole cross-section, with a mild decrease in the TMAZ. This can also be seen in the distribution of grain boundary misorientation angles, which run along a very similar path.

{111} PFs from individual weld areas are presented in Fig. 8. It can be noted that the texture is different for the three BMs. For both samples after plastic working, i.e. U and E + U, a shear texture with a dominant B {112}<110>, but also A and C components are present [25]. For both samples, the texture components are the same, only the intensity changes, since for the sample after the hybrid process a higher intensity is measured. Sample A was annealed, therefore traces of B texture are still present but at a lower intensity. It is commonly observed in samples annealed after being previously plastically deformed that their texture is preserved [26]. Textural changes are also observed across the welds. In the SZs, shear components are present. The crystal reference frame has been rotated to align with the local shear coordinate system – SPN and SD. The main components in a SZ are of B fiber type, i.e. B {112̄} <110̄> and B̄ {112̄} <110̄> [27].

### 3.2. Mechanical properties

Microhardness profiles for both planes, transverse and normal, are presented in Fig. 9. The average values for the BMs are as follows:  $27 \pm 1$  HV0.1,  $48 \pm 1$  HV0.1 and  $58 \pm 2$  HV0.1 in the transverse-sections for samples A, U and E + U, respectively. In the case of the normal plane, for the A and U samples the average value is comparable to that obtained in the transverse sections. However, in the case of sample E + U, the

Table 1 – Quantitative results of  $d$  and fraction of HAGBs for subsequent weld areas measured in the transverse and normal planes.

|        |          | Transverse plane      |          | Normal plane          |          |
|--------|----------|-----------------------|----------|-----------------------|----------|
|        |          | $d$ [ $\mu\text{m}$ ] | HAGB [%] | $d$ [ $\mu\text{m}$ ] | HAGB [%] |
| A–A    | BM       | $18.4 \pm 10.5$       | 78.7     | $20.3 \pm 13.1$       | 79.0     |
|        | HAZ/TMAZ | $5.2 \pm 5.5$         | 65.4     | $6.4 \pm 5.7$         | 63.2     |
|        | SZ       | $3.6 \pm 1.7$         | 81.8     | $4.2 \pm 2.6$         | 79.5     |
| U–U    | BM       | $1.1 \pm 1.3$         | 43.5     | $2.5 \pm 1.7$         | 40.9     |
|        | HAZ/TMAZ | $4.6 \pm 1.8$         | 64.4     | $3.9 \pm 1.5$         | 66.2     |
|        | SZ       | $4.4 \pm 1.2$         | 75.7     | $4.1 \pm 1.6$         | 78.3     |
| E + U- | BM       | $0.8 \pm 0.5$         | 79.1     | $1.5 \pm 1.1$         | 68.2     |
|        | HAZ/TMAZ | $3.3 \pm 1.1$         | 74.5     | $4.3 \pm 1.8$         | 63.4     |
|        | SZ       | $3.5 \pm 1.2$         | 77.4     | $4.9 \pm 1.9$         | 80.1     |

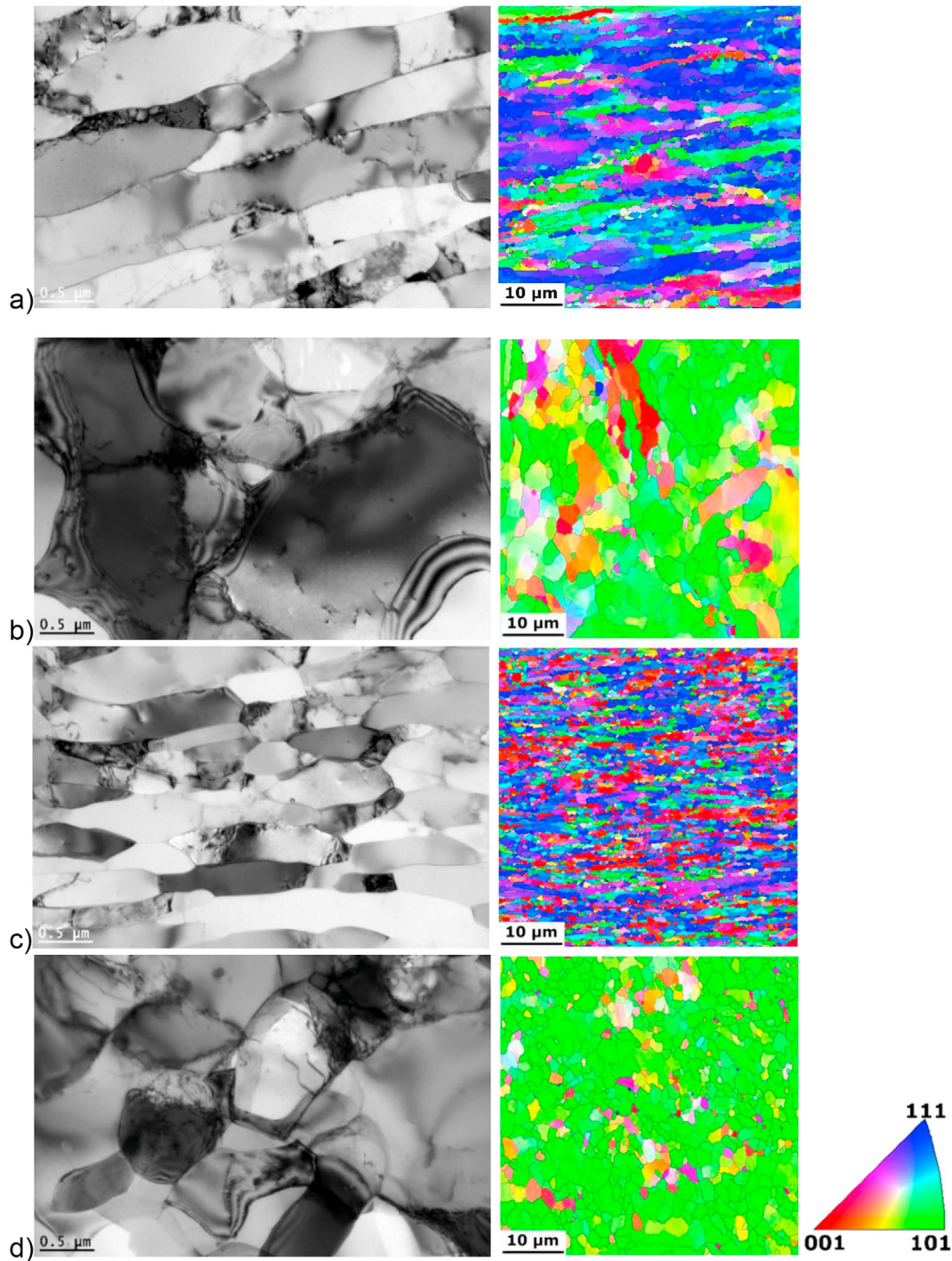


**Fig. 4 – Microstructure of BMs: a) U - transverse plane, b) U – normal plane, c) E + U – transverse plane and d) E + U – normal plane.**

average value of microhardness is lower, and equals  $54 \pm 1$  HV0.1. In the SZ in each weld, the microhardness is reduced to an average value of 31–32 HV0.1 for both planes. This represents a moderate increase in comparison with the BM of sample A, and a distinct decrease in relation to the BM of the samples after plastic working (see Table 1). The size of the SZ is estimated at about 10 mm (measurements were taken in the middle part of the samples in both planes examined). For the

A–A weld, it is not possible to precisely distinguish the HAZ and TMAZ, while for the U–U and E + U–E + U welds, this is an area where the microhardness decreases from the level in the BM to the SZ. The size of these zones is about 2 mm from each side, advancing and retreating, for the U–U weld, and about 2.5 mm for the E + U–E + U weld.

The representative engineering stress–strain curves for the welds and BMs are presented in Fig. 10. In the latter case,

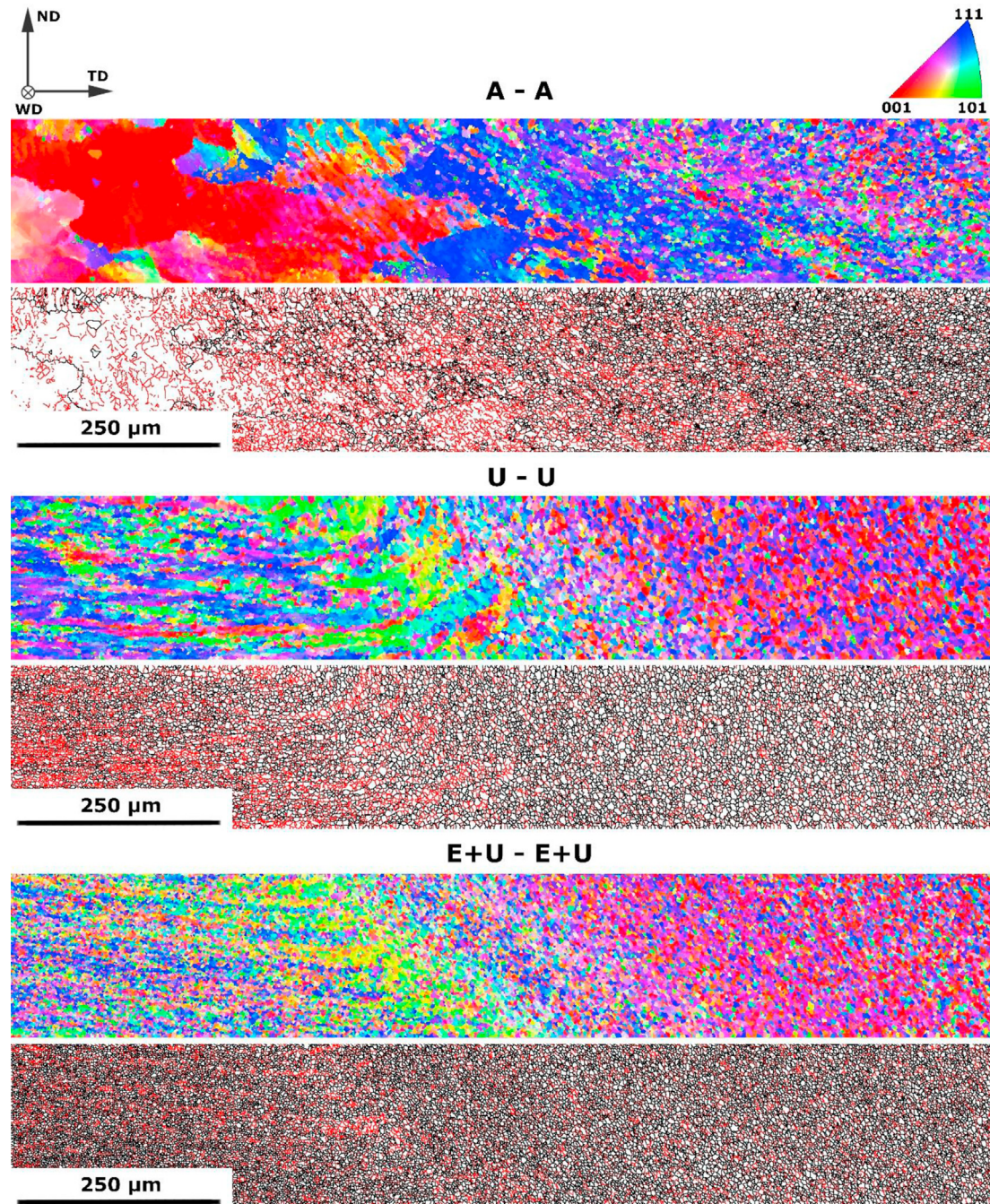


**Fig. 5 – OIMs and maps of grain boundaries of the transverse plane of welds: on the left – BM on advancing size, on the right - SZ.**

the maximum stress significantly increases with plastic deformation, but the elongation to break decreases. For sample A, the average values of UTS and E are  $78 \pm 4$  MPa and  $42 \pm 5\%$ , respectively. For sample U, these values are  $144 \pm 9$  MPa and  $11 \pm 2\%$ , and for sample E + U –  $195 \pm 7$  MPa and  $12 \pm 2\%$ . Such changes are typical for samples of varying grain size, since grain boundaries are a strengthening factor. For the A–A weld, the stress–strain curve coincides with the curve for the BM, as the rupture occurred in the BM of the welded samples (see Fig. 11b). For the U–U and E + U-E + U

welds, the curves differ from their BM, as the rupture takes place in the SZ. The UTS is reduced in comparison with samples U and E + U, and equals about 87 MPa for both welds, while E has a value of about 8%. However, it should be noted that the UTS values for the U–U and E + U-E + U welds are higher than for sample A and the A–A weld, which results from the smaller grain size in the SZ.

Strain 3D maps are shown in Fig. 11. For each weld two maps: (i) at the maximum stress (tensile strength) and (ii) at the rupture are presented. In the A–A weld, a strain

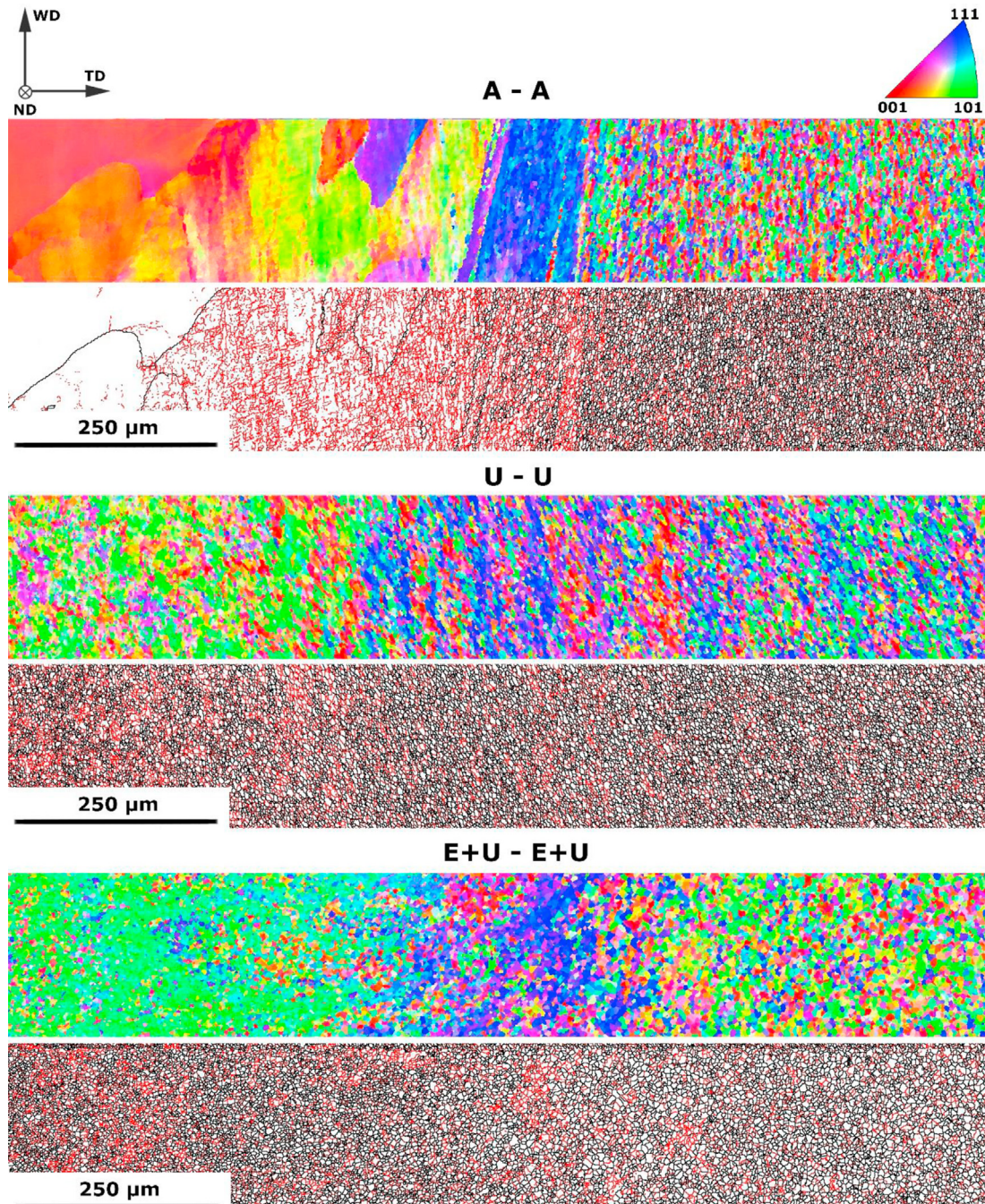


Fig. 6 – OIMs and maps of grain boundaries of the normal plane, on the left – BM on advancing size, on the right - SZ.

localization was obtained in the BM zone. The location of the rupture was not detected due to the limited area recorded during the tests. The SZ's deformation during the tensile test was negligible, as can be seen by the scale of the Lagrange strain. However, both the TMAZ and HAZ experienced straining. In the case of the U-U and E + U - E + U welds, the strain localization took place in the center area of the SZ. The rupture also occurred in this area and, in contrast to the results obtained for the A-A weld, the BMs and the HAZs and TMAZs as well were not deformed during testing. These results indicate that the welds were of good quality, since the

strain localization and rupture occurred in the areas with the biggest average grain size.

### 3.3. Electrochemical behaviour

The representative PP curves recorded in the BMs and SZs using 1 mm working electrode (surface area of  $7.85 \times 10^{-3} \text{ cm}^2$ ) are presented in Fig. 12. For the BMs, the  $E_{\text{CORR}}$  is in the range of  $-700 \pm 25 \text{ mV}_{\text{Ag/AgCl}}$ . It can be noticed that the surfaces of the samples are very active, as evidenced by the steep slope of the anodic branches and the sharp increase in the current density

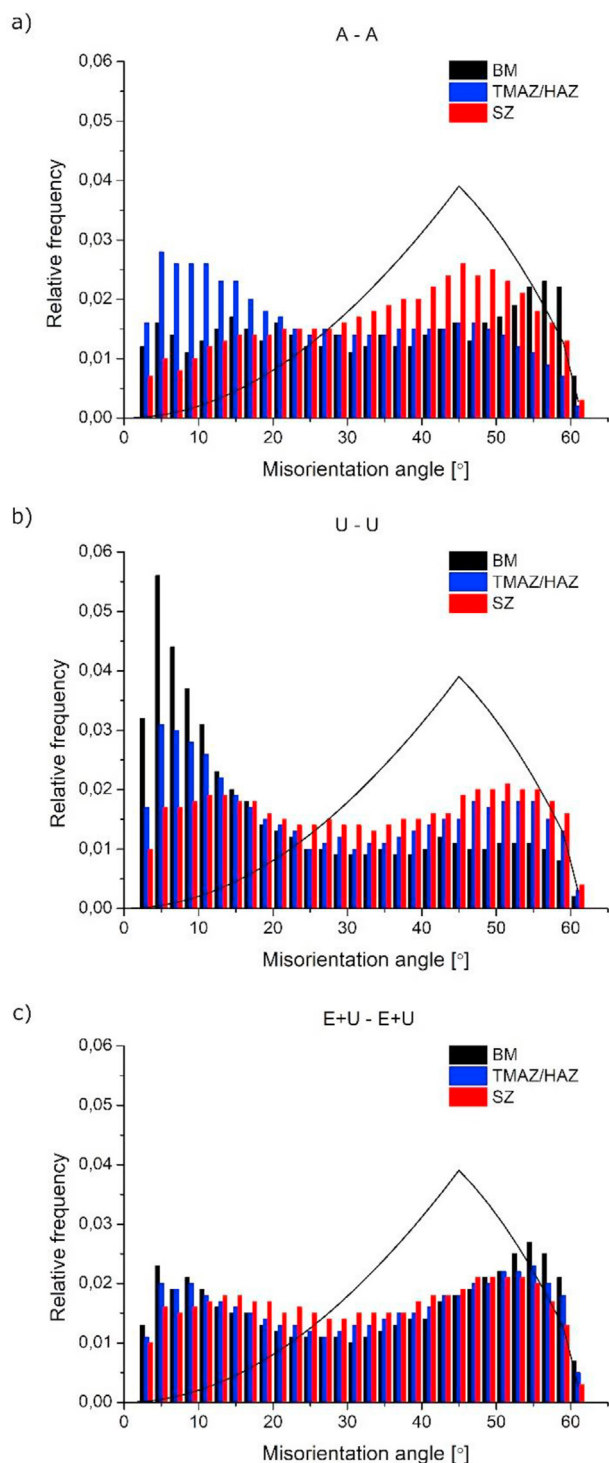


**Fig. 7 – Misorientation grain boundary distribution in transverse sections of welds: a) A–A, b) U–U, c) E + U–E + U; black line indicates theoretical Mackenzie plot.**

values. For the SZs, the  $E_{\text{corr}}$  is shifted towards more positive values, and ranges from about  $-670 \pm 20$  mV<sub>Ag/AgCl</sub>. In this case, the anodic branches show gentler slopes than the BMs. The surface morphology after the PP tests is presented in Fig. 13 for the BMs and in Fig. 14 for the SZs. Pitting corrosion

can be observed in all cases. The corrosion damage is significant, as is reflected by the high current density values. In the BMs, the area covered by pitting is larger than in the SZs. For the BMs, the percentage values of the area covered by pits are 23.8%, 19.2% and 22.2% for sample A, U and E + U, respectively. For the SZs of the welds from these materials, the area covered by pitting is lower, at 7.8%, 11.7% and 9.9%, respectively. The calculated values are approximate due to the large development of the pitting surface. Nevertheless, they show a trend, and that the corrosion damage on the surface is about twice as large for the BMs than for the SZs. In the SZs, separate pits can be observed, while for the BMs the corrosion attack progressed enough for the pits to merge. Moreover, the pit morphology is in agreement with the grain size and the distribution of HAGBs. For all SZs, the shape of the pits is close to equiaxial, while the cavities are spreading randomly around them, similarly to sample A, but with the difference that the corrosion attack is more pronounced in sample A. For samples U and E + U, the pits are more flattened and the cavities are located mainly horizontally, as are the locations of HAGBs (see Fig. 4).

Pitting corrosion initiates in the vicinity of inclusions or primary intermetallic particles due to the occurrence of microgalvanic couplings with the Al matrix. In the examined material, two types of particles were identified seen in Fig. 15: (i) Si inclusions of irregular shape and various sizes and lengths even up to 15  $\mu\text{m}$  and (ii)  $\text{Al}_3\text{Fe}$  primary intermetallic particles. The latter are round in shape and up to 5  $\mu\text{m}$  wide. An image of sample U after the PP tests, with both types of inclusions marked, is presented in Fig. 15. The initiation of pitting occurs in the vicinity of the inclusions and further dissolution of the material depends on other microstructural factors. Due to frictional forces during the FSW, the particles become shredded and fragmented, as presented in Fig. 15b for the SZ of the U–U weld. The size of the particles is significantly reduced, to a value below 200 nm. Also, their distribution becomes more homogeneous.

For a detailed characterization of the electrochemical properties of the samples, experiments were conducted using a microcapillary, which makes it possible to distinguish differences between all four zones. The representative PP curves are shown in Fig. 16. The size of the microcapillary cell was 250  $\mu\text{m}$  (surface area of  $5 \times 10^{-4}$  cm<sup>2</sup>). Two electrochemical parameters,  $E_{\text{corr}}$  and  $i_{\text{corr}}$ , are gathered in Fig. 17, where the average values from three measurements are presented. The curves differ from the results shown in Fig. 12 due to the different activity on the anodic branches. The corrosion potential remains at similar values, as does the  $i_{\text{corr}}$  (similar to that of the BM, see Fig. 12). However, the current density on the anodic branch does not increase as significantly as it does in a larger area of the working electrode. Nevertheless, in the case of the microcapillary as well, noise can be seen in the curves, indicating that metastable corrosion activities are taking place. From an analysis of the average values, there is an evident correlation between the position in the weld and the  $E_{\text{corr}}$  values. The general tendency is that this increased in the direction of the SZ. The biggest difference is observed for the A–A weld, where the difference between the BM and SZ is almost 40 mV. The HAZ and TMAZ have values in between. Moreover, considering only the BM, it can be observed that the

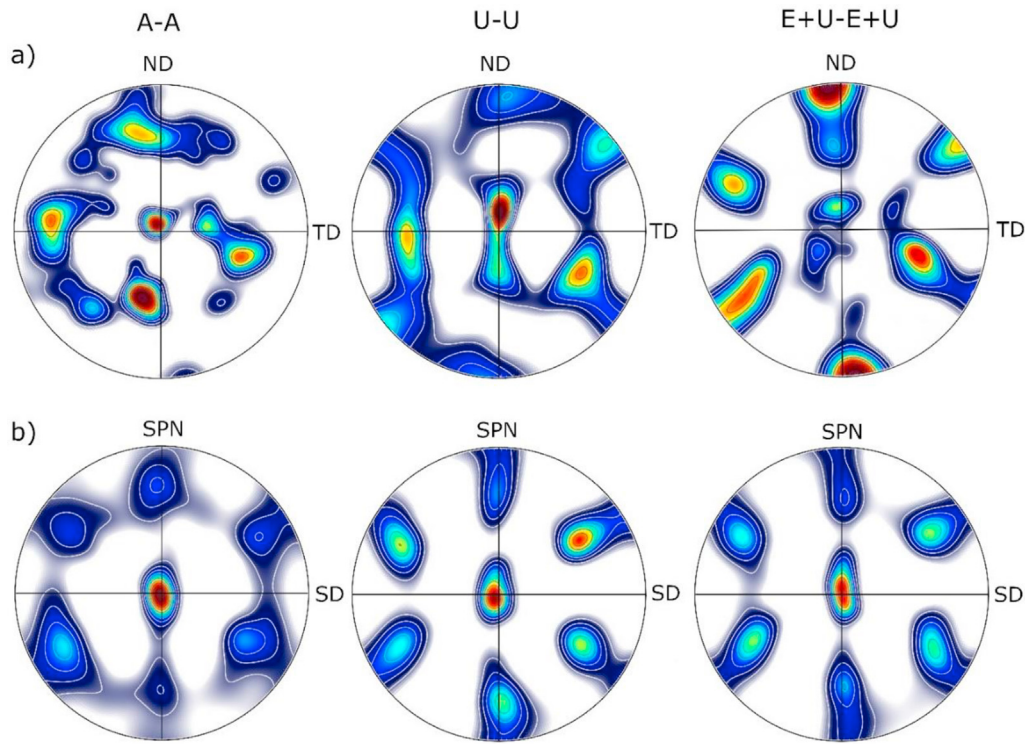


Fig. 8 – {111} PFs from a) BM and b) SZ.

$E_{corr}$  also increases with increasing sample deformation. In the case of the  $i_{corr}$ , there is a correlation for the A–A weld that the highest value is observed for the BM and decreases in the direction of the SZ. Nevertheless, all the values are similar and within the margin of error. It should only be pointed out that, for the SZs, the value of the  $i_{corr}$  is the most reproducible for each weld, indicating that this area has the most homogeneous microstructure.

The surfaces of the samples after PP using the micro-capillary is shown in Fig. 18. Similarly to the results obtained using a standard cell (Fig. 13 and Fig. 14), pitting corrosion is observed. When the surface area damaged by corrosion is calculated, it is seen that corrosion attack is less pronounced in comparison with the 1 mm cell. The highest value of surface covered in pits is achieved for the BM of the A–A weld, at

~7.5%. For the other samples, this value is comparable and the results are in a range of 3–4.5%, indicating negligible differences between the samples.

#### 4. Discussion

##### 4.1. Microstructure evolution and its influence on mechanical properties

Three materials were chosen for welding – annealed, cold worked via conventional metal forming, i.e. flat die upsetting, and after a hybrid SPD processing, i.e. mtECAP + multistroke upsetting. The BMs differed in grain size and shape, microtexture intensity, fraction of HAGBs, and (not examined in the

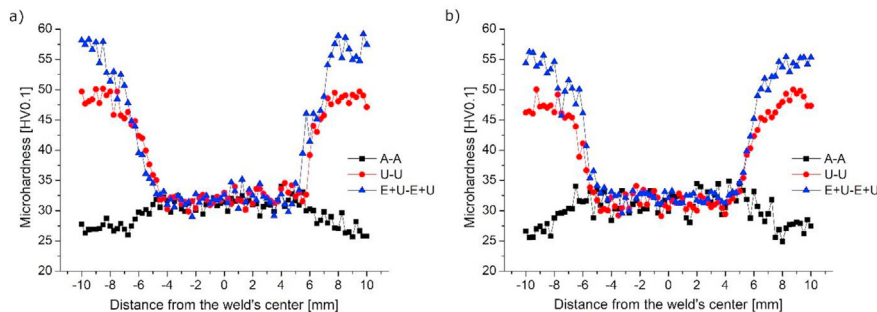
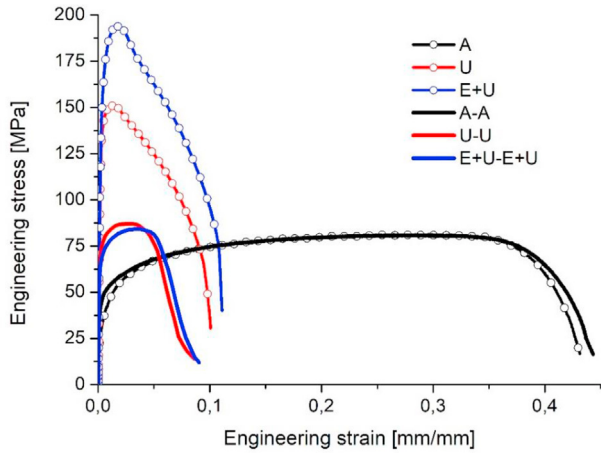


Fig. 9 – Microhardness profiles from welds a) transverse and b) normal planes; on the left side – advancing side, on the right side – retreating side.



**Fig. 10 – Representative stress–strain curves for welds and BMs.**

present study) dislocation density. The annealed sample featured equiaxial grains with a size of about 20  $\mu\text{m}$  and an HAGB fraction of 79%. Plastic working caused a significant grain refinement to a value below 1  $\mu\text{m}$ . However, due to the upsetting process, the grains on both samples, i.e. U and E + U, exhibited different shapes depending on which plane was examined. This was due to a flattening of the previously equiaxial grains. In the SZ, the grain shape and size were comparable in both planes, indicating that equiaxial grains a few microns across were obtained. Moreover, all three welds resulted in similar grain sizes.

Based on the microstructure observations, it can be stated that DRX occurred in the SZ. Intense plastic deformation at an elevated temperature is a well-established process for forming new grains in FSW joints [28]. It occurs in the SZ, where strain rates are in a range of  $10^1$ – $10^2$   $\text{s}^{-1}$ , while the peak temperature in this region is expected to be in a range from 0.6

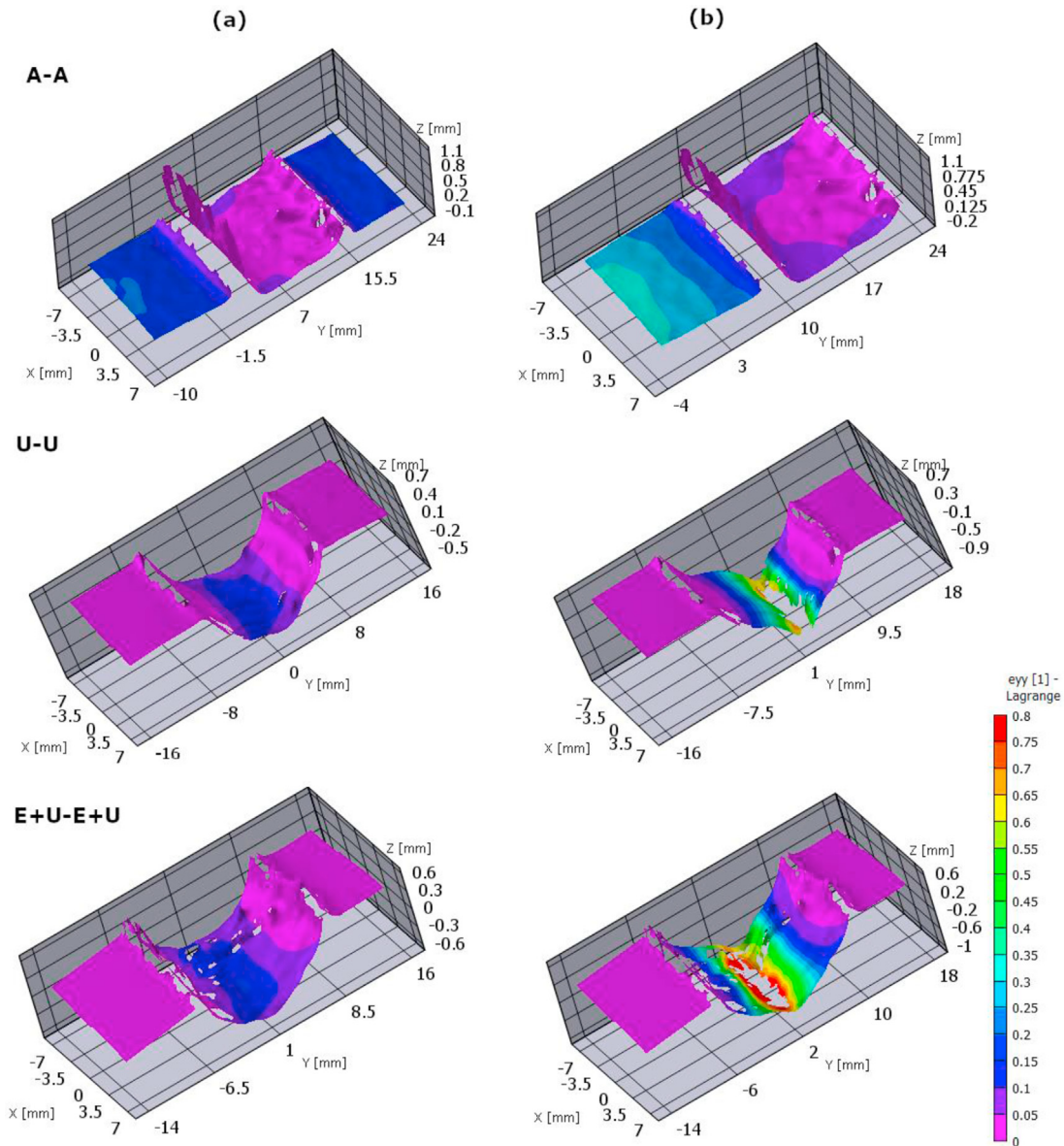


**Fig. 11 – 3D DIC deformation maps of welds recorded at a) maximum stress and b) rupture.**

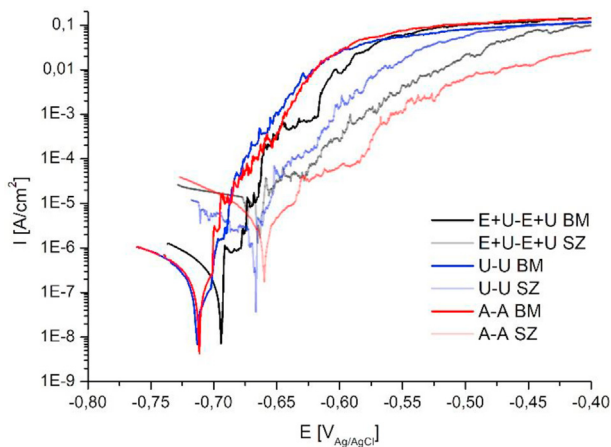


**Fig. 12 – Representative PP curves from measurements performed in the transverse sections of welds for the diameter of the working electrode of 1 mm.**

to  $0.95 T_{\text{melt}}$ , depending on the welding material and process parameters. In the case of Al and its alloys, the temperature usually does not exceed  $500\text{ }^{\circ}\text{C}$  ( $\sim 0.75 T_{\text{melt}}$ ), at which Al behaves as a thermoviscous material [29]. In a review [29], three models of the evolution of grain structure during FSW for Al alloys are presented – discontinuous dynamic recrystallization (DDRX), geometric dynamic recrystallization (GDRX), and continuous dynamic recrystallization (CDRX). DDRX occurs by the nucleation and growth of new grains, CDRX is based on the formation of arrays of LAGBs and a gradual increase in misorientation angles, while GDRX results from the impingement of serrated grain boundaries [30]. The dominant mechanism depends on what material is welded, and for alloys with high stacking fault energies (SFE), such as Al, that mechanism is mainly CDRX. Results from a Monte Carlo simulation together with the experimental results for commercially pure Al 1060 have shown that the main DRX mechanisms may also differ, depending on the side of the weld and the tool rotational speed, which affects the heat input level [31]. An increase in tool rotation speed results in a higher welding temperature. Thus the motion of grain boundaries is easier, which can prompt the occurrence of GDRX. Additionally, a higher strain rate and welding temperature can induce DDRX. At a lower tool rotation speed, a lower heat input is achieved, which promotes CDRX as a new grain formation process. CDRX is assumed to be the main restoration process in the present study. A characteristic feature of GDRX is the fibrous grains that remain in the SZ [5]. Moreover, DDRX is unlikely to occur in Al and its alloys because high SFE values simplify the cross-slip and the dislocation climb, which suppress the accumulation of the strain necessary for the nucleation and growth of grains [32]. CDRX, as in the present study, results in equiaxial grains with a high fraction of HAGBs in the SZ.

In order to confirm the restoration phenomena, the texture components observed in the SZ can be used. Recrystallization via particle-stimulated nucleation, which is based on the formation and growth of new grains around non-deformable

particles, leads to a random texture, as was shown for AA5083 after friction stir processing [28]. Whereas the distinct share texture components that are observed in the SZ indicate the occurrence of GDRX or CDRX. Similarly, in [33] CDRX occurred in a dissimilar weld of AA7003 and AA6060, which was also observed by a simple shear texture component in the SZ - B  $\{112\}\langle 110\rangle$ , as in the present study, while the BMs were characterized by different texture components – for BM 7003 it was cube  $\{100\}\langle 001\rangle$ , E  $\{111\}\langle 110\rangle$  and  $\{223\}\langle 122\rangle$ , while 6060 had a cube texture of  $\{100\}\langle 001\rangle$ . Moreover, in the TMAZ, a DRX and partially DRV occurred. In the HAZ, a static recovery was the main mechanism for the microstructure evolution. It resulted in grain structure similar to those of the BMs, while the fraction of LAGBs increased. In the present study as well, for the A–A weld an elevated number of LAGBs were observed in the transition zone between the BM and SZ (i.e. HAZ/TMAZ) (see Fig. 5 and Fig. 6).

The elevated number of microstructural defects after plastic working caused an increase in the mechanical properties. This was visible from the microhardness results, as for sample A on the transverse plane it was 27 HV0.1, while for samples U and E + U those values were 48 HV0.1 and 58 HV0.1, respectively. On the surface of sample E + U, this value differed due to differences in grain size. These changes are based on the well-known Hall–Petch equation [34], as an elevated number of grain boundaries causes a strengthening of the material. Therefore, changes in the welds cross-sections were observed. The microhardness profiles obtained for the examined welds (Fig. 9) are in accordance with the scheme presented in [6], where for the annealed material a mild increase was shown, while for the work-hardened material there was a decrease in the SZ. In the first case, when a weld was performed from annealed materials, the HAZ was indistinguishable, and there could be no, or just slight changes in hardness between the BM and SZ noted. A slight increase in microhardness was explained by the modest hot work hardening and grain refinement, which was also achieved in the present study. Also, since weld formation eliminates the prior deformation microstructure in a cold-worked material, the hardness of the nugget zone is independent of the original condition. The same relationship was observed for the U–U and E + U-E + U welds, where a decrease in microhardness was observed in the SZ. Moreover, comparable values in the SZs were obtained, independent of the initial condition of the BMs. Tensile tests confirmed the microhardness results, as the rupture occurred in areas with the lowest microhardness, which is in the SZ for the U–U and E + U-E + U welds, and in the BM for the A–A weld. Local changes in mechanical properties were also analyzed by means of straining maps, shown in Fig. 11. For the U–U and E + U-E + U welds, deformation was obtained only in the SZ, even grain size increased in the TMAZ and HAZ. In the case of the A–A weld, deformation took place over the entire length of the weld, although the rupture occurred in the BM.

The correlation between the microstructures of the BM and SZ is an important topic when UFG materials are joined. So far, only Sun et al. [35] have shown a clear correlation between these and how the initial microstructure influence the microstructure and properties in the SZ for commercially pure

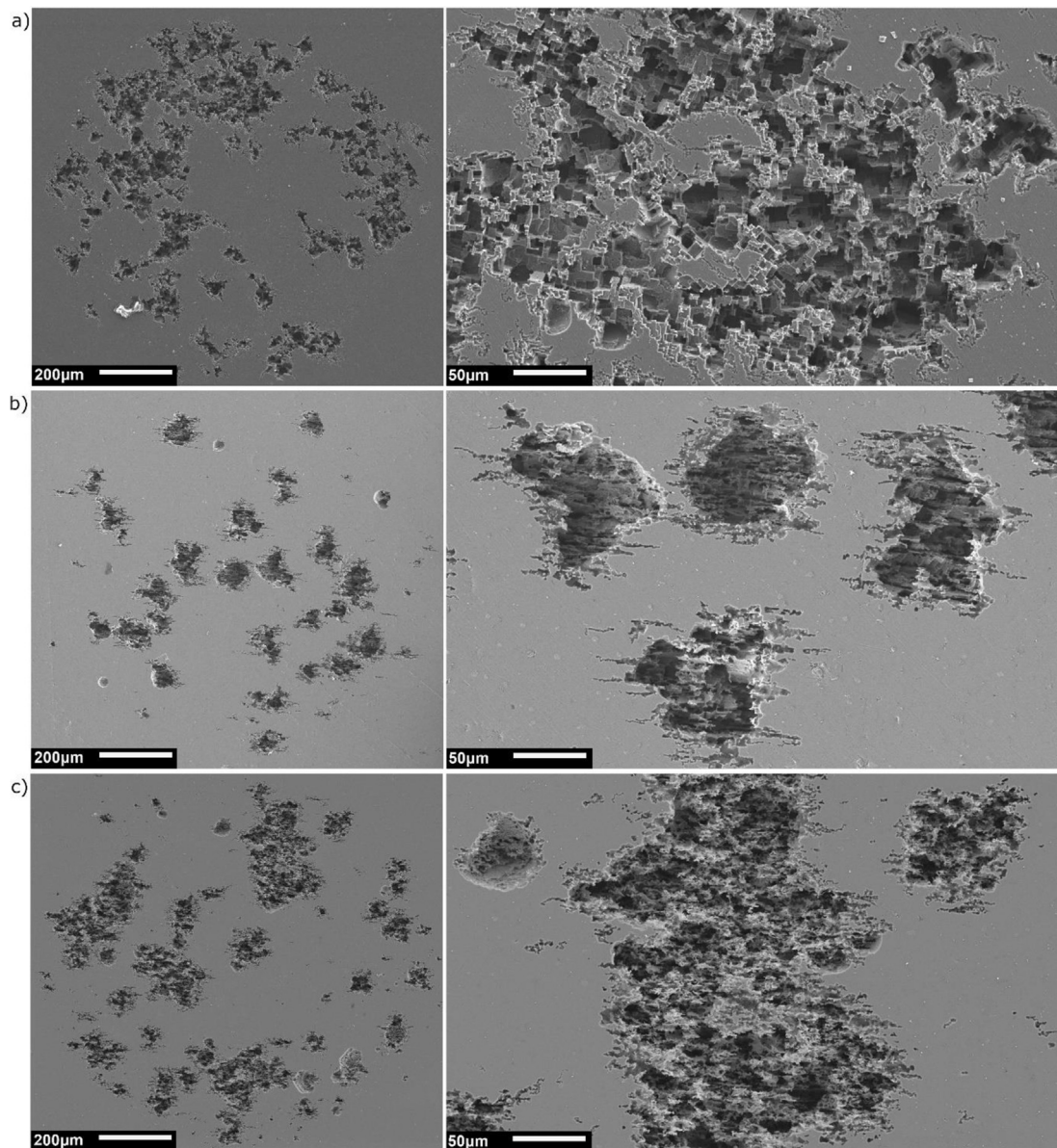


**Fig. 13 – SEM micrographs of the surface after PP tests of the BM: a) A, b) U, c) E + U.**

Al. They claim that the initial grain size influences the microstructure in the SZ of FSW-processed materials, as was shown in the microhardness profiles. For UFG Al a distinct decrease was observed, while the annealed sample having intermediate grain size was the most preferable for obtaining the highest hardness in the SZ. Nevertheless, no clear justification has been presented. In other works devoted to the welding of UFG commercially pure Al, results similar to those of the present study have been obtained with no correlation between the BM and SZ. As for UFG Al after constrained groove pressing, where microhardness changes in the SZ resulted only by changing the FSW parameters [36], not the initial condition of the BM. A decrease in microhardness in the SZ in comparison to the BM for UFG AA1050 and AA6016 was observed in [16], where the conclusion was that pre-deformation history has no influence on the resulting

microstructure or the mechanical properties within the SZ. Similarly, in the present study, based on the microstructure and microhardness profiles, it can be stated that the microstructure of the BM does not influence the microstructure and properties of the SZ. However, such an influence can be observed in the outer area, which is the TMAZ and mainly the HAZ. The size of the latter is directly connected with the process parameters and with the stability of the microstructure. In our previous work [14], it was showed that, as the deformation of the BM increases, so does the size of the HAZ. Similarly, in the present study, the size of the HAZ is bigger for the E + U-E + U weld than the U–U weld. It may be connected with the higher stored energy in the sample after the hybrid cold working process, whereby a lower activation energy could be needed for the recovery and recrystallization processes.

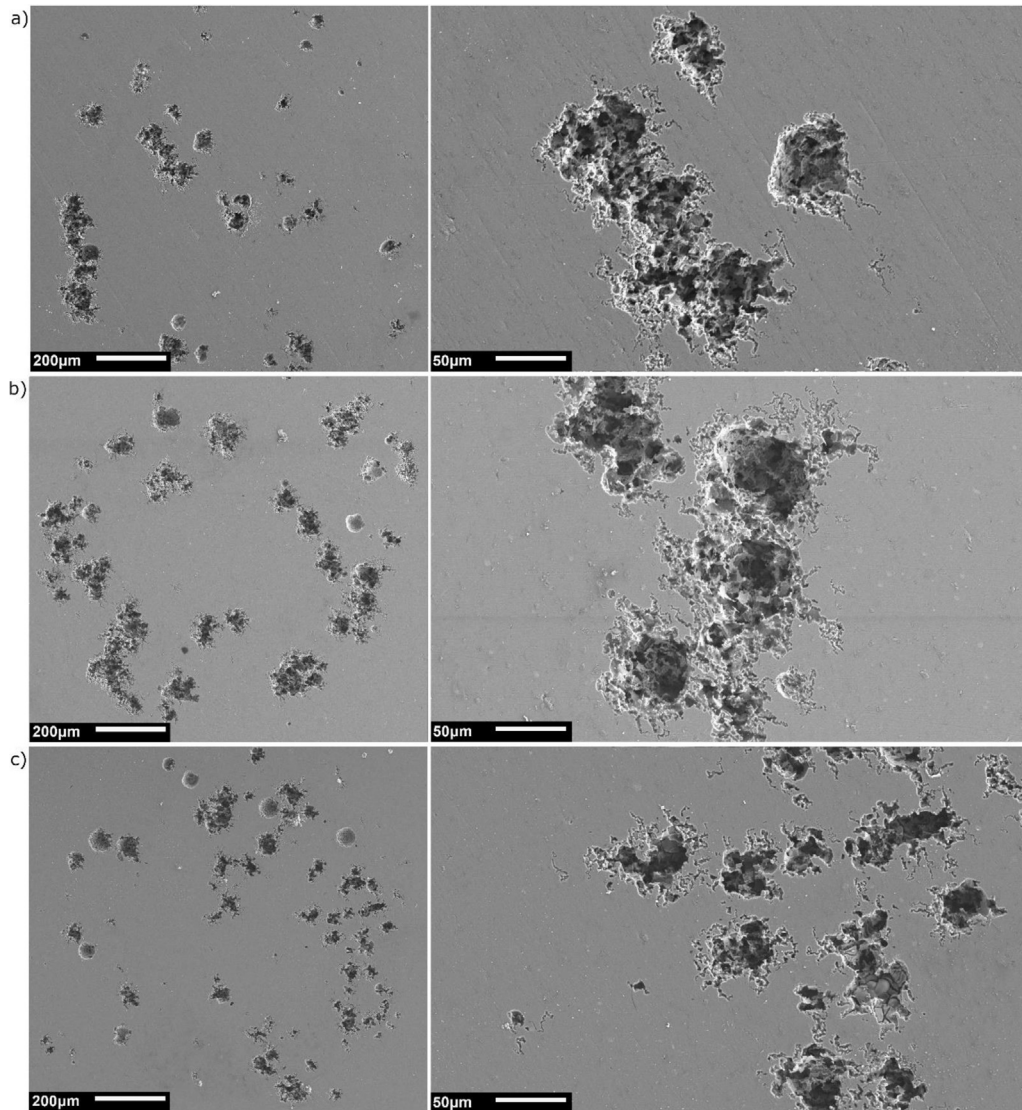


Fig. 14 – SEM micrographs of the surface after PP tests of the SZ: a) A, b) U, c) E + U.

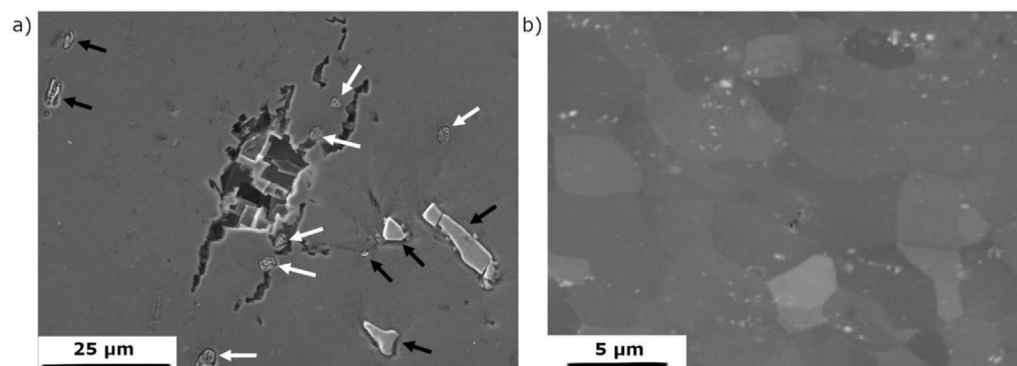
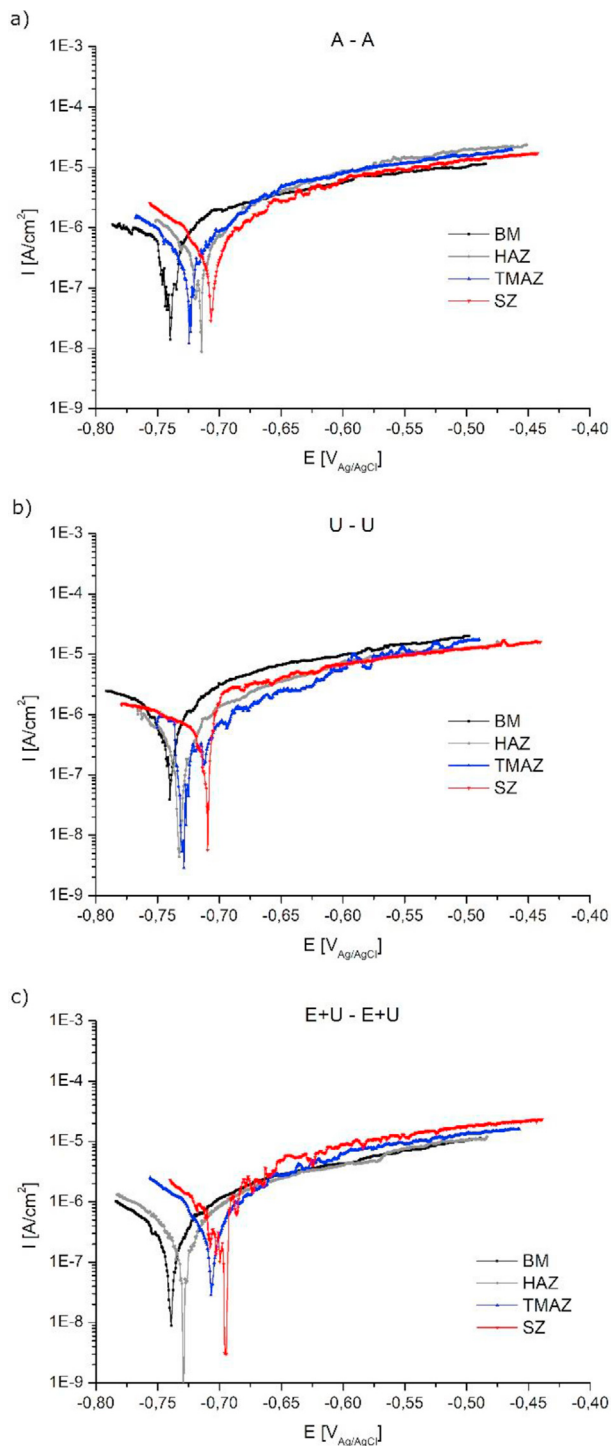


Fig. 15 – Surface of sample U: a) BM after the PP test (black arrows indicate Si inclusions, white arrows indicate Al<sub>3</sub>Fe intermetallic particles), and b) SZ with fragmented particles.



**Fig. 16** – Representative PP curves obtained in 3.5 wt.% NaCl of the particular welding zones for welds: a) A–A, b) U–U and c) E + U–E + U, using a microcapillary cell 250  $\mu\text{m}$  in size (surface area of  $5 \times 10^{-4} \text{ cm}^2$ ).

#### 4.2. Electrochemical behavior

Significant changes in microstructure across the weld influence the electrochemical properties. Susceptibility to corrosion attack has been examined for various Al alloys after the

FSW process. In work [37], a relationship between the grain size and the electrochemical behaviour of the SZ for AA2050 was identified. Nevertheless, it was not possible to draw an unequivocal conclusion, because the precipitation state was identified as the critical parameter. Similarly, in work [38] welds from Al–Cu–Li showed different electrochemical responses between the BM and SZ, although those changes were attributed to high activity of the precipitates, which differed depending on the weld zone. A comparison between the TMAZ and BM for dissimilar welds of AA2024 and AA7075 was investigated in [39]. The TMAZ experienced more severe localized corrosion during immersion tests in 3.5% NaCl, which was attributed to a higher stored energy than in the BM. Moreover, a more negative  $E_{\text{corr}}$  and larger  $i_{\text{corr}}$  were observed for the TMAZ, indicating lower corrosion resistance in this zone. It was attributed to the presence of second-phase particles that were responsible for the initiation of pitting.

Apart from the second-phase particles, primary intermetallic particles also play a dominant role in corrosion resistance. Their influence might be even more significant because they are larger than second-phase precipitates. This is crucial in the case of pitting corrosion since, due to the changes in electrochemical potential between such particles and the matrix, their interface is the place where corrosion initiates. In the examined material, two types of impurities were detected: (i) Si inclusions and (ii)  $\text{Al}_3\text{Fe}$  primary intermetallic particles (Fig. 15). Both of these are cathodic in character in relation to the anodic Al matrix [40,41], meaning that they promote the dissolution of the matrix in the vicinity of the particles. In the SZ, they can be shredded and uniformly distributed due to frictional forces. It was shown in [42], and it was also observed in the present study, where its size decreased significantly in the SZ (see Fig. 15b). The influence of intermetallic particles was investigated for FSW joints of 2524-T3 Al alloy in 0.05 M NaCl [43], whose authors observed no significant difference between the electrochemical behavior of the SZ and BM, although the BM corroded more due to the presence of primary intermetallic particles. In the SZ, the particles were fragmented and uniformly distributed, which resulted in a more chemically homogeneous microstructure and thereby improved overall corrosion resistance. In the present study, the higher  $i_{\text{corr}}$  in the SZ for the 1 mm working electrode may indicate that there was higher activity due to an elevated number of galvanic couplings. Nevertheless, the anodic activity was lower than in the BM, and this resulted in more pronounced corrosion attack on the BM. Microstructure homogeneity in the SZ may play a decisive role in this. In work [44], the increased intermetallic constituent particles during FSW caused an increase in the galvanic corrosion coupling, and thereby decreased the corrosion resistance of the weld regions in comparison with the BM. A different approach was taken by Nam et al., where the corrosion resistance of AA6061 after FSW was examined, but only in the SZ, and depending on the travelling speed applied in the welding process [45]. It was shown that a higher speed resulted in better corrosion resistance, which was attributed to a more significant grain refinement and microstructural homogeneity. It facilitated the formation of a corrosion resistant film on the FSW specimens due to a shift in positive  $E_{\text{corr}}$ , reduced  $i_{\text{corr}}$ , and increased film and charge transfer resistances. It was also

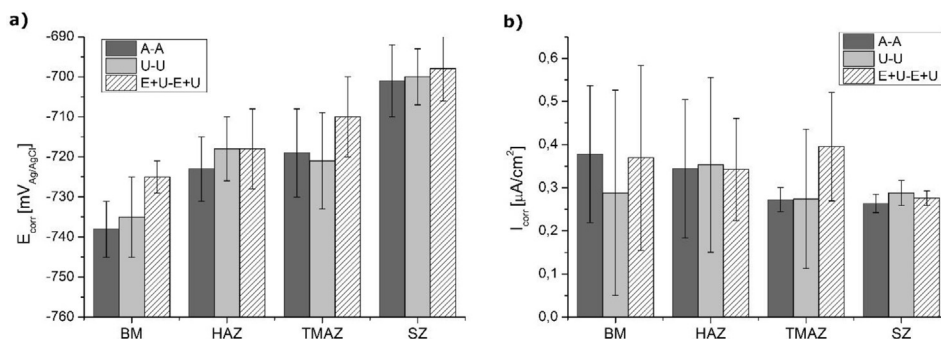


Fig. 17 – Graphs of the average values of a)  $E_{corr}$  and b)  $i_{corr}$ .

suggested that this result could be due to a homogeneous distribution of the impurities in the alloy caused by the FSW, on which a homogeneous passive film was formed that enhanced the material's corrosion resistance.

The use of a microcapillary cell to study the electrochemical behavior of FSW joints has been also employed in the past because it makes it possible to investigate individual weld zones. Changes can only be properly characterized if one zone is isolated from the others. Still, only a limited number of

works have taken such an approach. In work [46], a cell with an exposed area of  $0.035 \text{ cm}^2$  was used for the electrochemical investigation of dissimilar welds of two Al alloys, AA2024-T3 and AA7475-T651. Examinations in a  $0.01 \text{ mol NaCl}$  solution revealed increased corrosion activity in the SZ (e.g. higher current density) in comparison with the TMAZ/HAZ. This was attributed to galvanic coupling between the alloys in the SZ. Local corrosion behavior on FSW joints from Al–Cu–Li alloy was examined in [47], where for polarization scans the size of

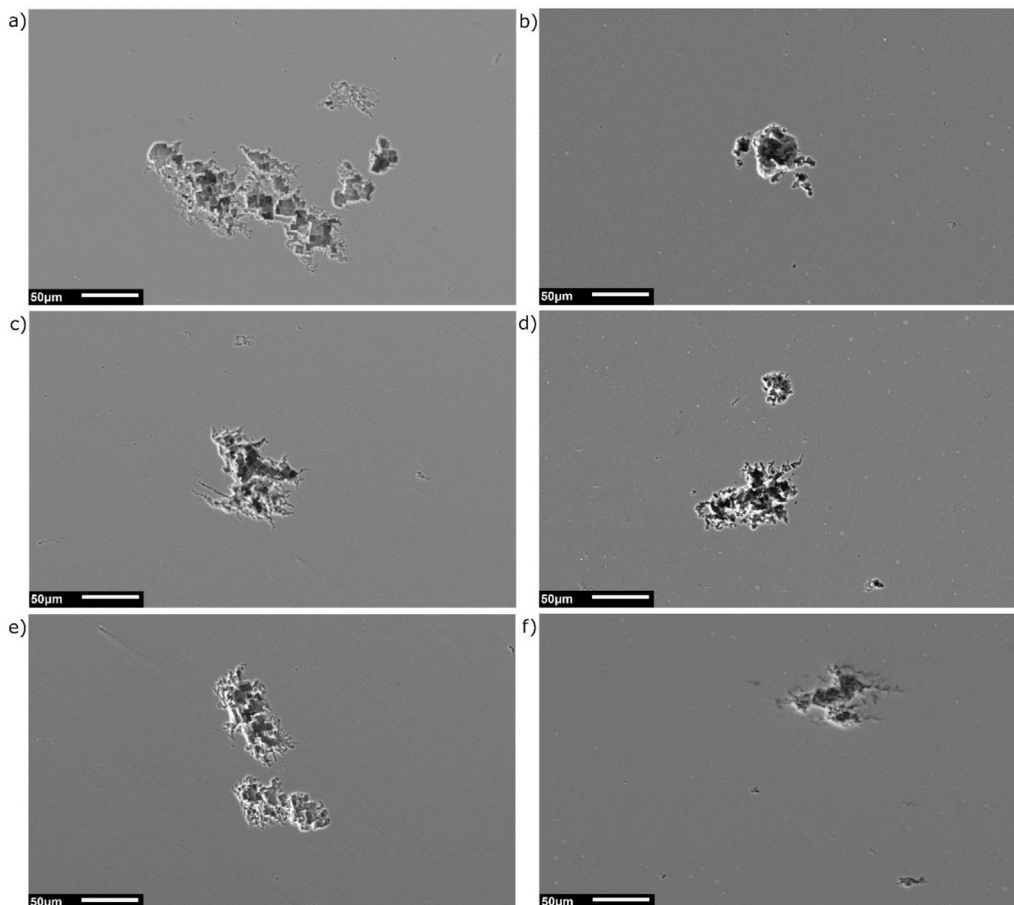


Fig. 18 – SEM micrographs after PP using a microcapillary of the A–A weld: a) BM and b) SZ, weld U–U: c) BM and d) SZ, weld E + U-E + U: e) BM and f) SZ.

the cell was  $0.20 \text{ cm}^2$ . The authors of that study distinguished differences between weld zones in a  $0.005\text{M NaCl}$  solution – the SZ displayed an  $E_{\text{corr}}$  that was about  $100 \text{ mV}$  higher, and slightly lower current densities and pseudo-passive behavior, which indicates higher corrosion resistance than for the HAZ. Higher anodic current densities are associated with faster dissolution. Both the SZ and HAZ areas were more susceptible to severe localized corrosion, which was attributed to the microgalvanic cells formed within these welded zones due to the presence of secondary phases in the 2098-T351 alloy and their interactions with the adjacent matrix. Electrochemical properties as a function of placing an FSW weld on Al 5456 alloy were investigated in [48] using a microelectrochemical cell with a  $1 \text{ mm}$  capillary to distinguish the size of the working electrode in a  $0.1 \text{ M NaCl}$  solution. The anodic reactivity was the most pronounced in the SZ, and was related to the presence of nano-scale precipitates dispersed throughout the matrix of the susceptible regions. In the present study, two sizes of working electrode were analyzed: (i)  $1 \text{ mm}$  and (ii)  $250 \mu\text{m}$ . The latter made it possible to distinguish differences between all four weld zones. Discrete changes were noticed. However, the  $E_{\text{corr}}$  was connected with the zone, since its value increased in all the welds in the direction of the SZ from the BM. Moreover, differences in the results were obtained: for the  $1 \text{ mm}$  working electrode the anodic activity was significantly higher than it was for the microcapillary, and there was a more significant corrosion attack on the sample surface. The influence of capillary size on the polarization curve was also observed in [49], where it is stated that, when the examined area is smaller, a lower number of constituent particles are present, and the anodic current is therefore significantly reduced. It was concluded that any differences between the macro and micro measurements are associated with the volume fraction of the particles in the material. This may explain the higher anodic activity in the present study, where the area of the working electrode was increased.

For both sizes of working electrode, differences between the examined zones were observed, and the SZs are assumed to have better corrosion resistance as the surface area covered with pitting was half that in the BMs. Higher activity was also evident in the higher anodic currents. When the microcapillary was applied, the differences between particular zones were more subtle, with decreased activity on the surface. Nevertheless, the SZs showed the highest  $E_{\text{corr}}$ . Moreover, the  $i_{\text{corr}}$  values were less diverse, indicating a higher degree of homogeneity, caused by the welding process. The changes between zones were the most evident from the grain size. When only the changes in this parameter are analyzed, as was shown in a review paper for high purity Al [50], a decrease in grain size causes an ennoblement of the  $E_{\text{corr}}$  and a decrease in the  $i_{\text{corr}}$ . It implies that the reduction in the  $i_{\text{corr}}$  is under anodic control. These results were explained by the fact that fine-grain structure are more reactive surfaces with respect to oxide formation. When the purity is lowered, the dependence is not unequivocal, and a decrease in corrosion resistance can also be observed with decreasing grain size, as was shown in review [51]. Also, improvement in corrosion resistance in chloride environment with reduced grain size was achieved in [52]. Nevertheless, in the case of welds, other components also change, such as the fraction of HAGBs and

LAGBs, microtexture, and residual stresses. In the latter case, tensile longitudinal residual stresses along the weld centerline are observed, and they decrease in the direction of the BM [53]. In our previous work we have shown that SPD processing does not change residual stress values significantly, although in the SZ of an FSW joint (performed with the same parameters as in the present study) the increase is significant, from  $50 \text{ MPa}$  for the BM to about  $100\text{--}200 \text{ MPa}$  [54]. Comparable values of tensile residual stresses were measured and modelled in [55]. Although, there is no work in the literature that directly investigates the influence of residual stresses on the corrosion resistance of FSW joints, there are works describing this influence after different treatments, such as laser shock peening. In work [56], a copper surface after this treatment was examined in  $3.5\% \text{ NaCl}$ . A shrinking and intertwining of the top-surface led to a more compact surface with minor roughness, and this resulted in an increase in the hardness and hydrophobicity of the Cu leading to a new surface with high corrosion resistance. The lower dissolution of the SZs in the present study may be caused by the enhanced microstructure homogeneity and the elevated tensile residual stresses in this zone.

---

## 5. Conclusions

In the present study, similar welds from commercially pure Al with different initial microstructure were prepared using the FSW method, and then characterized. The local changes that took place in microstructure, mechanical properties and corrosion resistance of the samples were thoroughly investigated, and the following conclusions can be drawn:

1. The microstructure of the BM does not affect the microstructure in the SZ. This is due to the CDRX that occurs during welding. In the SZ, equiaxial grains were obtained having an average size of  $3.5\text{--}5.0 \mu\text{m}$  in transverse and normal planes. The grain size for the BM varied from  $0.8 \mu\text{m}$  to  $20 \mu\text{m}$ . Changes in the microstructure were observed in the TMAZ and HAZ. For the A–A weld, these zones were characterized by an increased number of LAGBs, while for the U–U and E + U-E + U welds the number of grain boundaries was reduced in comparison with the BM due to a coarsening of the grains in the direction of the SZ.
2. As a result of the microstructure changes, the mechanical properties also evolve. The microhardness values in the SZ were the same for all welds. In comparison with the annealed sample this is a moderate increase, while in comparison with the samples after plastic working it is a decrease. The size of the TMAZ/HAZ transition zone was greater for the E + U-E + U weld. As to tensile strength, the welds from the samples after plastic deformation exhibited higher values, since the rupture occurred in the SZ, while for the weld from annealed Al the rupture was in the BM. Also, the differences in deformation during the tensile tests could be observed.
3. The local electrochemical experiments revealed that the SZ is the most corrosion resistant area in  $3.5\% \text{ NaCl}$ . The corrosion attack there was just half of what it was in the BM when the  $1 \text{ mm}$  cell was used. This was due to the

higher microstructure homogeneity obtained in the FSW process. The use of a microcapillary made it possible to distinguish the differences among particular weld zones. In each case, independent of the BM, the  $E_{\text{corr}}$  increased in the direction of the SZ. The differences were also obtained between BMs – plastic deformation slightly enhanced corrosion resistance and in the case of 250  $\mu\text{m}$  cell the corrosion damage for A sample was almost twice as big as for samples U and E + U.

### Data availability

The raw/processed data required to reproduce these findings cannot be shared at this time as the data also forms part of an ongoing study.

### Declaration of Competing Interest

The authors declare that they have no known competing financial interests or personal relationships that could have appeared to influence the work reported in this paper.

### Acknowledgements

The authors would like to acknowledge the financial support received from the National Science Centre (Poland) under project number 2020/36/C/ST5/00162. The FSW experiments were conducted at TU Graz and supported by the KMM-VIN fellowship programme. We would like to thank Professor Lech Olejnik of WUT for helping with plastic working of the samples. Also, we would like to thank Dr. Tomasz Brynk of WUT, who currently works at SCK CEN in Mol, Belgium, for helping with the tensile tests.

### REFERENCES

- [1] Mishra RS, Ma ZY. Friction stir welding and processing. *Mater Sci Eng R Rep* 2005;50:1–78. <https://doi.org/10.1016/j.mser.2005.07.001>.
- [2] Heidarzadeh A, Mironov S, Kaibyshev R, Çam G, Simar A, Gerlich A, et al. Friction stir welding/processing of metals and alloys: a comprehensive review on microstructural evolution. *Prog Mater Sci* 2021;117:100752. <https://doi.org/10.1016/j.pmatsci.2020.100752>.
- [3] Meng X, Huang Y, Cao J, Shen J, dos Santos JF. Recent progress on control strategies for inherent issues in friction stir welding. *Prog Mater Sci* 2021;115:100706. <https://doi.org/10.1016/j.pmatsci.2020.100706>.
- [4] Du C, Wang X, Pan Q, Xue K, Ni M, Liu J. Correlation between microstructure and mechanical properties of 6061-T6 double-side FSW joint. *J Manuf Process* 2019;38:122–34. <https://doi.org/10.1016/j.jmapro.2019.01.010>.
- [5] Zeng XH, Xue P, Wu LH, Ni DR, Xiao BL, Wang KS, et al. Microstructural evolution of aluminum alloy during friction stir welding under different tool rotation rates and cooling conditions. *J Mater Sci Technol* 2019;35:972–81. <https://doi.org/10.1016/j.jmst.2018.12.024>.
- [6] Threadgill PL, Leonard AJ, Shercliff HR, Withers PJ. Friction stir welding of aluminium alloys. *Int Mater Rev* 2009;54:49–93. <https://doi.org/10.1179/174328009X411136>.
- [7] Jariyaboon M, Davenport AJ, Ambat R, Connolly BJ, Williams SW, Price DA. The effect of welding parameters on the corrosion behaviour of friction stir welded AA2024-T351. *Corrosion Sci* 2007;49:877–909. <https://doi.org/10.1016/j.corsci.2006.05.038>.
- [8] Maggiolino S, Schmid C. Corrosion resistance in FSW and in MIG welding techniques of AA6XXX. *J Mater Process Technol* 2008;197:237–40. <https://doi.org/10.1016/j.jmatprotec.2007.06.034>.
- [9] Grover HS, Chawla V, Brar GS. Comparing mechanical and corrosion behaviour of TIG & FSW weldments of AA5083-H321. *Indian J Sci Technol* 2017;10(45):1–8. <https://doi.org/10.17485/ijst/2017/v10i45/113537>.
- [10] Sinhmar S, Dwivedi DK. A study on corrosion behavior of friction stir welded and tungsten inert gas welded AA2014 aluminium alloy. *Corrosion Sci* 2018;133:25–35. <https://doi.org/10.1016/j.corsci.2018.01.012>.
- [11] Xie Y, Meng X, Wang F, Jiang Y, Ma X, Wan L, et al. Insight on corrosion behavior of friction stir welded AA2219/AA2195 joints in astronautical engineering. *Corrosion Sci* 2021;192:109800. <https://doi.org/10.1016/j.corsci.2021.109800>.
- [12] Valiev RZ, Estrin Y, Horita Z, Langdon TG, Zehetbauer MJ, Zhu Y. Producing bulk ultrafine-grained materials by severe plastic deformation. *JOM (J Occup Med)* 2006;58:33–9. <https://doi.org/10.1007/s11837-016-1820-6>.
- [13] Xie Y, Meng X, Li Y, Mao D, Wan L, Huang Y. Insight into ultra-refined grains of aluminum matrix composites via deformation-driven metallurgy. *Compos Commun* 2021;26:100776. <https://doi.org/10.1016/j.coco.2021.100776>.
- [14] Lipińska M, Olejnik L, Pietras A, Rosochowski A, Bazarnik P, Goliński J, et al. Microstructure and mechanical properties of friction stir welded joints made from ultrafine grained aluminium 1050. *Mater Des* 2015;88. <https://doi.org/10.1016/j.matdes.2015.08.129>.
- [15] Orłowska M, Brynk T, Huetter A, Goliński J, Enzinger N, Olejnik L, et al. Similar and dissimilar welds of ultrafine grained aluminium obtained by friction stir welding. *Mater Sci Eng* 2020;777:139076. <https://doi.org/10.1016/j.msea.2020.139076>.
- [16] Topic I, Hoppel HW, Goken M. Friction stir welding of accumulative roll-bonded commercial-purity aluminium AA1050 and aluminium alloy AA6016. *Mater Sci Eng* 2009;503:163–6. <https://doi.org/10.1016/j.msea.2007.12.057>.
- [17] Nikulin I, Malopheyev S, Kipelova A, Kaibyshev R. Effect of SPD and friction stir welding on microstructure and mechanical properties of Al-Cu-Mg-Ag sheets. *Mater Lett* 2012;66:311–3. <https://doi.org/10.1016/j.matlet.2011.08.104>.
- [18] Lipińska M, Olejnik L, Lewandowska M. A new hybrid process to produce ultrafine grained aluminium plates. *Mater Sci Eng* 2018;714:105–16. <https://doi.org/10.1016/j.msea.2017.12.096>.
- [19] Lewandowska M, Chrominski W, Lipinska M, Olejnik L, Rosochowski A. Incremental ECAP as a method to produce ultrafine grained aluminium plates. *Key Eng Mater* 2016;710:59–64. <https://doi.org/10.4028/www.scientific.net/KEM.710.59>.
- [20] Wejrzanowski T, Pielaszek R, Opalińska A, Matysiak H, Łojkowski W, Kurzydłowski KJ. Quantitative methods for nanopowders characterization. *Appl Surf Sci* 2006;253:204–8. <https://doi.org/10.1016/j.apsusc.2006.05.089>.
- [21] Beausir B, Fundenberger JJ. Analysis tools for electron and X-ray diffraction. ATEX - software; 2017. [www.atex-software.eu](http://www.atex-software.eu).

- [22] Suter T, Bohini H. Microelectrodes for studies of localized corrosion processes. *Electrochim Acta* 1998;43:2843–9.
- [23] Kamikawa N, Huang X, Tsuji N, Hansen N. Strengthening mechanisms in nanostructured high-purity aluminium deformed to high strain and annealed. *Acta Mater* 2009;57:4198–208. <https://doi.org/10.1016/j.actamat.2009.05.017>.
- [24] Mackenzie JK. Second paper on statistics associated with random disorientation of cubes. *Biometrika Trust* 1958;45:229–40.
- [25] Liu FC, Nelson TW. In-situ grain structure and texture evolution during friction stir welding of austenite stainless steel. *Mater Des* 2017;115:467–78. <https://doi.org/10.1016/j.matdes.2016.11.066>.
- [26] Montheillet F, Cohen M, Jonas J. Axial stresses and texture development during the torsion testing of Al, Cu and a-Fe. *Acta Metall* 1984;32:2077–89.
- [27] Fonda RW, Bingert JF. Texture variations in an aluminum friction stir weld. *Scripta Mater* 2007;57:1052–5. <https://doi.org/10.1016/j.scriptamat.2007.06.068>.
- [28] McNelley TR, Swaminathan S, Su JQ. Recrystallization mechanisms during friction stir welding/processing of aluminum alloys. *Scripta Mater* 2008;58:349–54. <https://doi.org/10.1016/j.scriptamat.2007.09.064>.
- [29] Jacquin D, Guillemot G. A review of microstructural changes occurring during FSW in aluminium alloys and their modelling. *J Mater Process Technol* 2021;288:116706. <https://doi.org/10.1016/j.jmatprotec.2020.116706>.
- [30] Heidarzadeh A, Asadi P. Microstructural evolution. In: *Adv. Frict. Stir Weld. Process.*; 2014. p. 65–140. <https://doi.org/10.1533/9780857094551.65>.
- [31] Yu P, Wu CS, Shi L. Analysis and characterization of dynamic recrystallization and grain structure evolution in friction stir welding of aluminum plates. *Acta Mater* 2021;207. <https://doi.org/10.1016/j.actamat.2021.116692>.
- [32] Khorrami MS, Kazeminezhad M, Miyashita Y. The correlation of stir zone texture development with base metal texture and tool-induced deformation in friction stir processing of severely deformed aluminum. *Metall Mater Trans* 2017;48:188–97. <https://doi.org/10.1007/s11661-016-3812-0>.
- [33] Dong J, Zhang D, Luo X, Zhang W, Zhang W, Qiu C. EBSD study of underwater friction stir welded AA7003-T4 and AA6060-T4 dissimilar joint. *J Mater Res Technol* 2020;9:4309–18. <https://doi.org/10.1016/j.jmrt.2020.02.056>.
- [34] Hansen N. Hall–Petch relation and boundary strengthening. *Scripta Mater* 2004;51:801–6. <https://doi.org/10.1016/j.scriptamat.2004.06.002>.
- [35] Sun Y, Fujii H, Takada Y, Tsuji N, Nakata K, Nogi K. Effect of initial grain size on the joint properties of friction stir welded aluminum. *Mater Sci Eng* 2009;527:317–21. <https://doi.org/10.1016/j.msea.2009.07.071>.
- [36] Khorrami MS, Kazeminezhad M, Kokabi AH. Mechanical properties of severely plastic deformed aluminum sheets joined by friction stir welding. *Mater Sci Eng* 2012;543:243–8. <https://doi.org/10.1016/j.msea.2012.02.082>.
- [37] Proton V, Alexis J, Andrieu E, Delfosse J, Lafont MC, Blanc C. Characterisation and understanding of the corrosion behaviour of the nugget in a 2050 aluminium alloy Friction Stir Welding joint. *Corrosion Sci* 2013;73:130–42. <https://doi.org/10.1016/j.corsci.2013.04.001>.
- [38] de Souza Carvalho Machado C, Donatus U, Milagre MX, Araujo JV de S, de Viveiros BVG, Klumpp RE, et al. How microstructure affects localized corrosion resistance of stir zone of the AA2198-T8 alloy after friction stir welding. *Mater Char* 2021;174:111025. <https://doi.org/10.1016/j.matchar.2021.111025>.
- [39] Zhang C, Huang G, Liu Q. Research on local corrosion behavior of thermo-mechanically affected zone in dissimilar AA2024/7075 friction stir welds. *Intermetallics* 2021;130:107081. <https://doi.org/10.1016/j.intermet.2020.107081>.
- [40] Buchheit RG. A compilation of corrosion potentials reported for intermetallic phases in aluminum alloys. *J Electrochem Soc* 1995;142:3994. <https://doi.org/10.1149/1.2048447>. 3396.
- [41] Birbilis N, Buchheit RG. Electrochemical characteristics of intermetallic phases in aluminum alloys. *J Electrochem Soc* 2005;152:B140–51. <https://doi.org/10.1149/1.1869984>.
- [42] Lipińska M, Ura-Bińczyk E, Olejnik L, Rosochowski A, Lewandowska M. Microstructure and corrosion behavior of the friction stir welded joints made from ultrafine grained aluminum. *Adv Eng Mater* 2017;19:1–10. <https://doi.org/10.1002/adem.201600807>.
- [43] Moreto JA, dos Santos MS, Ferreira MOA, Carvalho GS, Gelamo RV, Aoki IV, et al. Corrosion and corrosion-fatigue synergism on the base metal and nugget zone of the 2524-T3 Al alloy joined by FSW process. *Corrosion Sci* 2021;182:109253. <https://doi.org/10.1016/j.corsci.2021.109253>.
- [44] Gharavi F, Matori KA, Yunus R, Othman NK, Fadaeifard F. Corrosion behavior of Al6061 alloy weldment produced by friction stir welding process. *J Mater Res Technol* 2015;4:314–22. <https://doi.org/10.1016/j.jmrt.2015.01.007>.
- [45] Nam ND, Dai LT, Mathesh M, Bian MZ, Thu VTH. Role of friction stir welding – traveling speed in enhancing the corrosion resistance of aluminum alloy. *Mater Chem Phys* 2016;173:7–11. <https://doi.org/10.1016/j.matchemphys.2016.02.004>.
- [46] Bugarin AFS, De Abreu CP, Terada M, De Melo HG, Costa I. Effect of friction stir welding (FSW) on the electrochemical behavior and galvanic coupling of AA2024-T3 and AA7475-T651. *Mater Today Commun* 2020;25:101591. <https://doi.org/10.1016/j.mtcomm.2020.101591>.
- [47] da Silva RMP, Izquierdo J, Milagre MX, Betancor-Abreu AM, de Oliveira LA, Antunes RA, et al. On the local corrosion behavior of coupled welded zones of the 2098-T351 Al-Cu-Li alloy produced by Friction Stir Welding (FSW): an amperometric and potentiometric microelectrochemical investigation. *Electrochim Acta* 2021;373:137910. <https://doi.org/10.1016/j.electacta.2021.137910>.
- [48] Fonda RW, Pao PS, Jones HN, Feng CR, Connolly BJ, Davenport AJ. Microstructure, mechanical properties, and corrosion of friction stir welded Al 5456. *Mater Sci Eng* 2009;519:1–8. <https://doi.org/10.1016/j.msea.2009.04.034>.
- [49] Amar H, Vignal V, Krawiec H, Josse C, Peyre P, Silva SN, et al. Influence of the microstructure and laser shock processing (LSP) on the corrosion behaviour of the AA2050-T8 aluminium alloy. *Corrosion Sci* 2011;53:3215–21. <https://doi.org/10.1016/j.corsci.2011.05.066>.
- [50] Ralston KD, Fabijanic D, Birbilis N. Effect of grain size on corrosion of high purity aluminium. *Electrochim Acta* 2011;56:1729–36. <https://doi.org/10.1016/j.electacta.2010.09.023>.
- [51] Ralston KD, Birbilis N. Effect of grain size on corrosion: a Review. *Corrosion* 2010;66:1–4. <https://doi.org/10.5006/1.3462912>.
- [52] Xie Y, Meng X, Mao D, Qin Z, Wan L, Huang Y. Homogeneously dispersed graphene nanoplatelets as long-term corrosion inhibitors for aluminum matrix composites. *ACS Appl Mater Interfaces* 2021;13:32161–74. <https://doi.org/10.1021/acsmi.1c07148>.
- [53] Williams SW, Steuwer a. Residual stresses in friction stir welding. Woodhead Publishing Limited; 2010. <https://doi.org/10.1533/9781845697716.2.215>.
- [54] Brynk T, Orłowska M, Lewandowska M. Application of 3D DIC-assisted residual stress measurements for friction stir welding weld from ultrafine-grained aluminum. *Metall*

- Mater Trans A Phys Metall Mater Sci 2021;52:20–5. <https://doi.org/10.1007/s11661-020-06069-5>.
- [55] Buglioni L, Tufaro LN, Svoboda HG. Thermal cycles and residual stresses in FSW of aluminum alloys: experimental measurements and numerical models. *Procedia Mater Sci* 2015;9:87–96. <https://doi.org/10.1016/j.mspro.2015.04.011>.
- [56] Chukwuike VI, Echem OG, Prabhakaran S, Anandkumar S, Barik RC. Laser shock peening (LSP): electrochemical and hydrodynamic investigation of corrosion protection pre-treatment for a copper surface in 3.5 % NaCl medium. *Corrosion Sci* 2021;179:109156. <https://doi.org/10.1016/j.corsci.2020.109156>.